



Universidad Autónoma
de Madrid

Biblos-e Archivo
Repositorio Institucional UAM

Repositorio Institucional de la Universidad Autónoma de Madrid

<https://repositorio.uam.es>

Esta es la **versión de autor** del artículo publicado en:

This is an **author produced version** of a paper published in:

Applied Materials Today 26 (2022): 101384

DOI: <https://doi.org/10.1016/j.apmt.2022.101384>

Copyright: © 2022 Elsevier Ltd. This manuscript version is made available under the CC-BY-NC-ND 4.0 licence <http://creativecommons.org/licenses/by-nc-nd/4.0/>

El acceso a la versión del editor puede requerir la suscripción del recurso

Access to the published version may require subscription

Covalent organic frameworks based on electroactive naphthalenediimide as active electrocatalysts toward oxygen reduction reaction

Marcos Martínez-Fernández,^{‡a} Emiliano Martínez-Periñán,^{‡b} Sergio Royuela,^c José I.

*Martínez,^d F. Zamora,^{cefg} Encarnación Lorenzo^{*bfg} and José L. Segura^{*a}*

^a Departamento de Química Orgánica I, Facultad de CC. Químicas, Universidad

Complutense de Madrid, 28040 Madrid, Spain. E-mail: segura@ucm.es

^b Departamento de Química Analítica y Análisis Instrumental, Facultad de Ciencias,

Universidad Autónoma de Madrid, 28049 Madrid, Spain.

E-mail: encarnacion.lorenzo@uam.es

^c Departamento de Nanoestructuras, Superficies, Recubrimientos y Astrofísica

Molecular, Instituto de Ciencia de Materiales de Madrid (ICMM-CSIC),

28049 Madrid, Spain

d Departamento de Química Inorgánica, Facultad de Ciencias, Universidad

Autónoma de Madrid, 28049 Madrid, Spain.

e Instituto Madrileño de Estudios Avanzados en Nanociencia (IMDEA-Nanociencia),

Cantoblanco, 28049 Madrid, Spain

f Institute for Advanced Research in Chemical Sciences (IAdChem), Universidad

Autónoma de Madrid, 28049 Madrid, Spain

g Condensed MatterPhysics Center (IFIMAC), Universidad Autónoma de Madrid,

28049 Madrid, Spain

‡ These authors contributed equally to this work.

<https://doi.org/10.1016/j.apmt.2022.101384>

Keywords

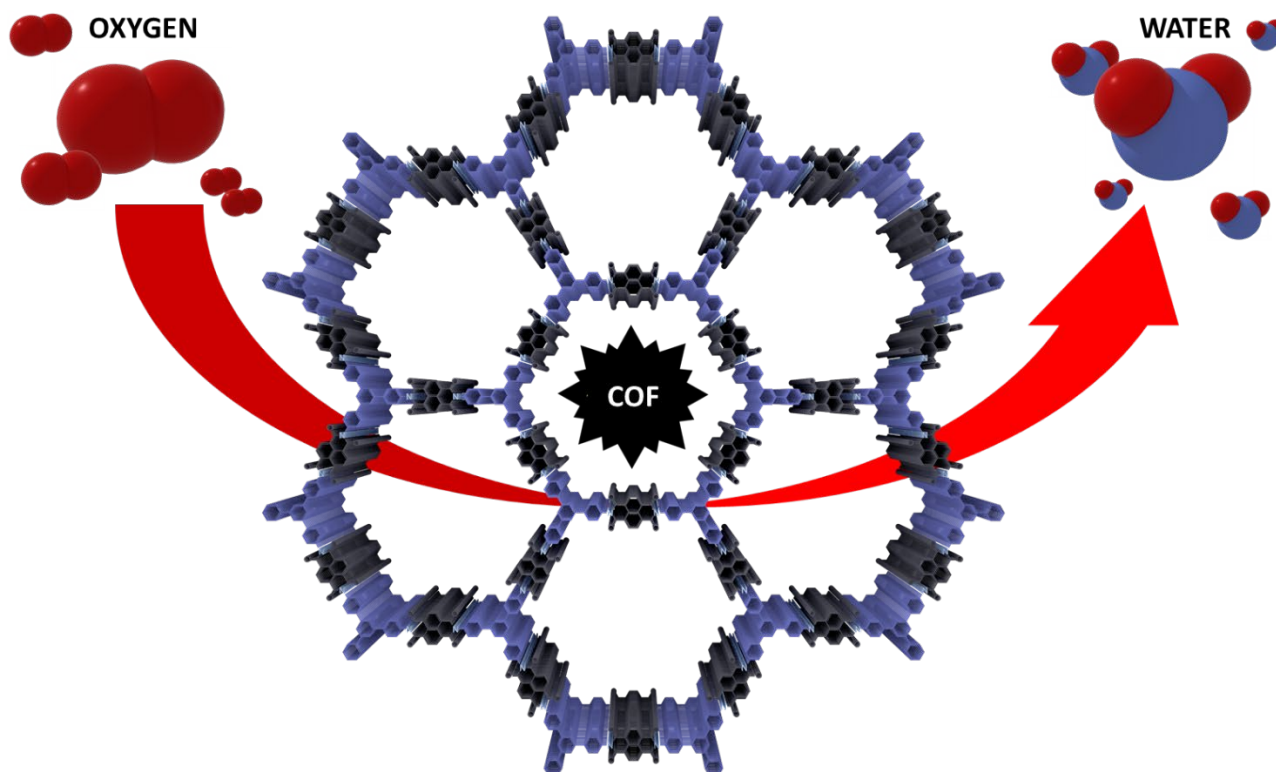
COF, covalent organic frameworks, naphthalenediimide, electrocatalysis, oxygen reduction reaction, metal-free, pyrolysis-free

Abstract

Developing organic electrocatalysts toward the oxygen reduction reaction (ORR) that avoid heteroatom doping processes and high-temperature carbonization is of great significance for the maturing of fuel cell applications. Herein, a series of two-dimensional imide-based covalent organic framework (COFs) electrocatalysts toward the ORR is reported. The hydrodynamic

electrochemical study reveals that 3.5 electrons are exchanged during the ORR indicating that the process catalyzed by these COFs has a clear preference for the 4-electron reduction pathway. The COFs contain conjugated electroactive naphthalenediimide (NDI) moieties that provides the active sites for the electrocatalysis and promotes the formation of COFs with face-to-face π - π stacked structures to provide intrinsic porosity and large surface areas. These COFs can be essentially considered as an organized pattern of active sites embedded in the pore walls of the COF. The choice of suitable comonomers with variable distortions from planarity offer the possibility of obtaining these electroactive COFs with similar redox ability but different degrees of porosity and interlaminar spacing. This work evidences a new insight into developing novel families of electrocatalysts from COFs. Structure and stacking fashion of the COF-systems are investigated on the basis of DFT calculations, as well as the photoabsorption spectra of the representative molecular entities and a proof-of-concept rationalization of the intermediate steps of the ORR mechanism

Graphical abstract



1. Introduction

Despite the difficulty to break the O=O bond in molecular oxygen because of its high bond energy of 498 kJmol^{-1} [1], the oxygen reduction reaction (ORR) is a key process not only in hydrogen peroxide generation but mainly in biological respiration and energy conversion. Therefore, the electrochemical reduction of molecular oxygen normally requires the assistance of an electrocatalyst to lower the energy barrier for the bond activation and cleavage. Different electrocatalysts can be used which are often classified attending to the followed pathways [2] which are mainly two in aqueous media: (i) a two-electron pathway is involved in the reduction of O_2 into H_2O_2 and (ii) a four-electron pathway takes place in the direct reduction of O_2 into H_2O .

A lower energy conversion is obtained in the two-electron reduction pathway that produces incomplete oxygen reduction and generates hydrogen peroxide as reaction product. Although the generation of free radicals and reaction intermediates used to have a negative impact on the activity of electrocatalysts,[3] due to the current interest in the development of methods for the electrochemical generation of H_2O_2 , efficient electrocatalysts for this process are currently under demand.[4] On the other hand, due to the higher electric current obtained in comparison with the two-electron pathway, the four-electron pathway used to be the desired one in energy conversion applications such as air batteries and fuel cells which are receiving a great deal of attention to be used for obtaining clean energy for vehicles, residential applications, and stationary power systems.[5] In the more promising fuel cell devices, the proton exchange membrane fuel cells (PEMFCs), oxygen is reduced at the cathode while hydrogen is oxidized at the anode. Following these redox processes, generated protons are transferred from the anode to the cathode through the electrolyte membrane while the electrons are transported over an external circuit load.[6] The anode hydrogen oxidation reaction as well as the cathode ORR traditionally occur on the surfaces

of platinum (Pt)-based catalysts.[7] However, the platinum production and its worldwide reserves are very limited. Furthermore, the cathodes used for ORR in PEMFCs are more than six orders of magnitude slower than the anodes for hydrogen oxidation and therefore high amounts of electrocatalysts must be included in cathode fabrication, thus increasing the costs.[5] In addition, the presence of Pt-based poisons and the generation of stable Pt–OH and Pt–O species slow the ORR kinetics and reduce the energy conversion efficiency.[8]

Despite the use of alternatives of platinum (Pt)-based catalysts that include transition-metal based materials, such as perovskite oxides,[9] transition metal borides/nitrides/oxides[10] layered metal hydroxides [11,12] and metal alloys,[13,14] there is a pressing need for the development of novel non-Pt and metal-free electrocatalysts for the ORR in the production of energy conversion devices.[15-18] Among them, carbon-based materials have stood out as promising alternative electrocatalysts for ORR because of the carbon global abundance and low cost. In this respect, some pure carbons have already shown ORR electrocatalytic activities similar to those of Pt and exhibit great stability, good electrical conductivity and high surface/volume ratio.[19-22] However, heteroatom doping processes and high-temperature carbonization are usually required to prepare these materials for which an accurate confirmation and precise tuning of active sites are still a challenge.[23,24] In order to face these challenges, a rational design followed by a precise synthesis of the electrocatalysts is highly advantageous. Thus, organic materials are receiving increasing attention as electrocatalysts given that the versatility of organic chemistry allow the controllable introduction of heteroatoms (B, P, N, O, S, F) and great structural tunability, paving the way for novel electrocatalytic mechanisms, and for the tuning of the desired two- or four-electron pathways.[23,25-30] In this respect, covalent organic frameworks (COFs) are an emerging class of highly crystalline materials with tunable pore sizes and large surface areas based

on frameworks linked by strong covalent bonds with excellent mass transport ability.[31-33] They present a good potential to provide a precise control for the locations of electrochemically active sites. Furthermore, the choice of proper synthesis routes, linkage motifs and building blocks allow the synthesis of programmable COF electrocatalysts[34-36] which have been already used for the hydrogen evolution reaction (HER),[37,38] the oxygen evolution reaction (OER)[39] and the oxygen reduction reaction (ORR).

COFs already used as electrocatalysts for the oxygen reduction reaction include heterometallic macrocycles-containing COFs and their derivatives,[40,41] COF-based nanohybrids [42] or carbonized metal-free COFs.[43-46] Taking into account that (i) the uncontrollable pyrolysis process may cause the structure collapse and result in elusive active sites and (ii) that metal-free organic materials are specially interesting for economic and environmental reasons,[47] the current challenge in the field involves the development of non-carbonized, pristine metal-free COFs as ORR electrocatalysts. Recently, the pioneering work of Jishan Wu and colleagues demonstrated that a low lying LUMO energy level promotes a favorable interaction with oxygen and triggers electrocatalytic activity. [48] Furthermore, inspiration is drawn from heteroatomic-doped graphene and carbon derivatives, which present carbonyl groups (such as carboxylates, anhydrides, quinones or imides) conjugated with an aromatic structure that can serve as electrochemically active centers for catalyzing the ORR process.[49] It can be envisaged that a straightforward strategy to enhance the performance of pristine metal-free COFs as ORR electrocatalysts may involve the introduction of this type of electrocatalytic active units into the framework. As we have recently shown, a low lying LUMO naphthalenediimide-based COF is an efficient metal-free electrocatalyst for the oxygen reduction.[50] This type of COF can be

essentially considered as an organized pattern of active sites embedded in the pore walls of the COF.

For this purpose, in this article we want to further explore the potential of using naphthalenediimide-based COFs as electrocatalysts for the oxygen reduction reaction and we report the electrocatalytic activity of a series of two-dimensional (2D) imide-based COFs containing electroactive naphthalenediimide (NDI) units (TAPX-NDI-COFs, Scheme 1). The materials have been designed to have the following characteristics: (i) they must have intrinsic porous structures to facilitate ion transport thus enhancing the reaction rate, (ii) large surface areas are highly desirable to provide enough active sites to be involved in the catalytic reactions and (iii) the presence of π -conjugated NDI moieties may improve the charge carrier transport and serve as electrocatalytic active units for the oxygen reduction reaction.

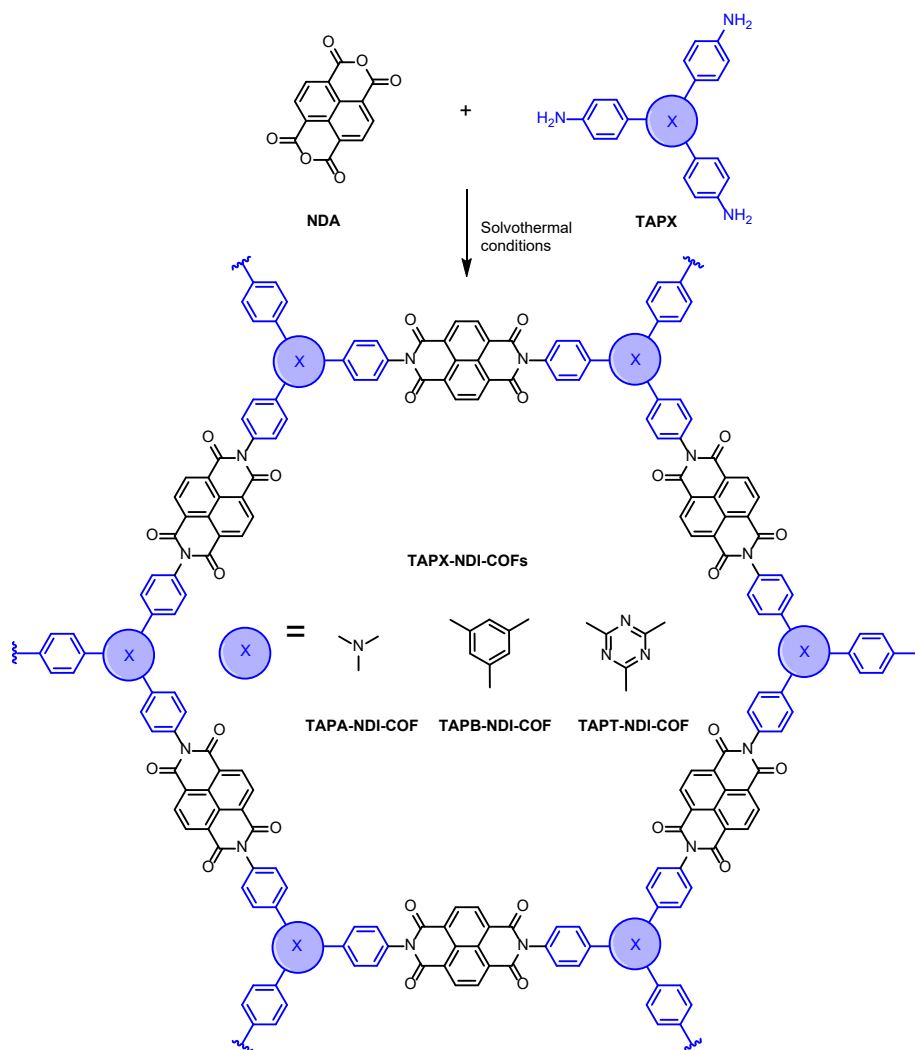
Together with the electroactive naphthalenediimide moieties, three different trigonal nodes are incorporated in the COF structure with different degrees of distortion from planarity. In addition to the slightly distorted 1,3,5-triphenylbenzene (TAPB) moiety used as knot in our preliminary study,[50] we incorporate now a planar 2,4,6-triphenyl-*s*-triazine (TAPT), and a triphenylamine (TAPA) which is significantly distorted from planarity. The combination of monomers with C_3 and C_2 geometries and complementary functionalities provide a series of hexagonal COFs in which the planarity of the nodes is tuned by choice of the three different trigonal systems. A combined UV-vis, electrochemical and theoretical study is carried out to analyze the effect of the different distortion from planarity of the trigonal units on the interlaminar spacing and porosity in the COF. In addition, the suitability of using these electroactive COFs with similar redox ability but different degrees of porosity and interlaminar spacing for electrocatalytic purposes in the ORR is also explored.

2. Materials and methods

2.1. Reagents

The following reagents were commercially available and were used as received: 1,4,5,8-naphthalenetetracarboxylic dianhydride (NDA), *p*-nitroacetophenone, tris-4-nitrophenylamine, 4-aminebenzonitrile, trifluoromethanesulfonic acid, palladium on carbon (10 wt%), hydrazine hydrate (50-60 wt%), platinum on carbon (10 wt%), *N,N'*-dimethylformamide (DMF), *N*-methyl-2-pyrrolidone (NMP), mesitylene, tetrahydrofuran (THF), *n*-hexane, NaOH, tetrabutylammonium perchlorate (TBAP) for electrochemical measurements, chloroform (CHCl₃), ethanol (EtOH). TAPA, TAPB and TAPT triamine compounds (TAPX) were synthesized by previously reported literature (supporting information).

2.2. TAPX-NDI-COF synthesis



Scheme 1. Syntheses of TAPX-NDI-COFs under the following solvothermal reaction conditions: TAPA-NDI-COF: 180 °C, 3 days, uncatalyzed; TAPB-NDI-COF: 120 °C, 4 days, 1 % isoquinoline; TAPT-NDI-COF: 150 °C, 4 days, 1 % isoquinoline.

The novel TAPT-NDI-COF (screening conditions are summarized in table S1), as well as the previously reported TAPA-NDI-COF[51] and TAPB-NDI-COF[50] have been synthesized by condensation reactions between 1,4,5,8-naphthalenetetracarboxylic dianhydride NDA and the corresponding TAPX triamine derivative (Scheme 1) under solvothermal reaction conditions by heating the reaction mixtures in a vacuum-sealed Pyrex vessel. TAPX-NDI-COFs were obtained as insoluble powders which were subsequently washed (supporting information) and characterized

by powder X-ray diffraction (PXRD), solid state ^{13}C cross-polarization magic angle spinning NMR (^{13}C -CP-/MAS-NMR), Fourier-transform infrared spectroscopy (FTIR), sorption isotherms, thermo-gravimetric analysis (TGA) and elemental analysis.

2.3. TAPX-NDI molecular analogues (TAPX-NDI-A)

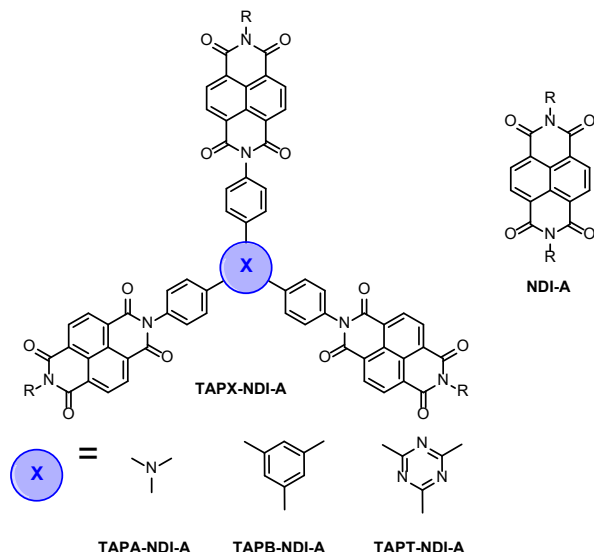


Figure 1. Chemical structure of the COFs' molecular analogues TAPX-NDI-A of the and the NDI-A molecule (R = Alkyl chain) used as molecular systems for comparison purposes.

For comparison purposes, molecular analogues TAPA-NDI-A, TAPB-NDI-A and TAPT-NDI-A (Fig. 1) have been synthesized by condensation reaction between naphthalenemonoimide (NMI) and the corresponding triamine derivatives TAPX (Supporting Information). These molecular systems have been characterized by nuclear magnetic resonance (^1H and ^{13}C -NMR), mass spectrometry (MS) and FTIR. Additionally, the basic dialkyl substituted naphthalimide unit NDI-A [52] (Figure 2), as well as the NMI[53], has been obtained by imidation condensation reaction between NDA and the corresponding aliphatic amine compound according to previous reported procedures.[53,54]

2.4. Instrumental

Solids were analysed by FTIR on a Bruker TENSOR 27 on a diamond plate (ATR). PXRD measurements were carried out with X'PERT MPD with conventional Bragg-Brentano geometry using monochromatic Cu K α 1 radiation ($\lambda = 1.5406 \text{ \AA}$) in the $2\theta = 2^\circ - 40^\circ$ range. ^{13}C CP/MAS NMR spectra were recorded on a Bruker AVANCE III HD-WB 400 MHz with a rotation frequency of 12 kHz. N_2 sorption isotherms. N_2 (77 K) adsorption-desorption measurements were carried out on a Micromeritics Tristar 3000. Samples were previously activated for 4 h under high vacuum ($<10^{-7}$ bar) at 120°C . TGA was performed on a TGA-Q50 instrument on a platinum plate, heating the samples under nitrogen atmosphere at a heating rate of $10^\circ\text{C}/\text{min}$. Solution ^1H NMR and ^{13}C NMR spectra were recorded on a Bruker AVIII-300 MHz spectrometer. Chemical shifts were reported in ppm and referenced to the residual non-deuterated solvent frequencies (CDCl_3 : δ 7.26 ppm for ^1H , 77.0 ppm for ^{13}C). Mass spectra were recorded by means of matrix-assisted laser desorption/ionization time-of-flight (MALDI-TOF) or fast atom bombardment (FAB) ionization techniques. Transmission electron microscopy (TEM). TEM micrographs were recorded in a JEOL JEM 1400 TEM at 200 kV. Scanning electron microscopy (SEM) were recorded in a JEOL JSM7600F. Ultraviolet-Visible (UV-vis) spectrums were recorded in a Varian Cary 50 scan spectrometer. Bipotentiostat PGSTAT302N MBA (MetrohmAutolab) and NOVA 1.11 software were used for electrochemical measurements.

2.5. Electrochemical measurements

Electrochemical measurements with no-agitation were carried out in a glass and Teflon homemade cell. Glassy Carbon electrodes 0.3 cm of diameter from CH Instruments (GC) were used as working electrodes. As counter electrode a graphite bar electrode was employed. As reference electrode a homemade saturated calomel electrode (SCE) was used. At first, the

electrochemical behaviour of TAPX-NDI-As were study in solution of 0.1 M CHCl_3 containing 0.7 mM of each analogue. The electrochemical activity of GC electrode modified with TAPX-NDI-COFs were also analysed. For this porpoise, a suspension of each COF materials (1 mg/mL) and Super P carbon (1 mg/mL) in a mixture EtOH/ H_2O (7/3) were prepared. After 30 min of sonication in a bath, 5 μL of the obtained suspension were drop-casted over GC electrode. The electrodes were dried, and the electrochemical activities were measured in 0.1 M TBAP/ CHCl_3 . Same procedure was employed to modified electrodes and study the electrochemical behaviour of COFs materials in 0.1 M NaOH in the presence and the absence of dissolved O_2 . In the case of TAPX-NDI-As, Glassy carbon (GC) electrodes were modified by dropcasting an aqueous suspension of the Super P carbon (1 mg/mL) followed by the subsequent drop-casted deposition of the solutions containing the TAPX-NDI-A (0.14 mM) in CHCl_3 .

Hydrodynamic measurements were made using a glassy carbon disk/platinum ring RRDE electrode from PINE and the same counter and reference electrode as in static measurements were employed. Measures were made in a conventional electrochemical cell adapted to RRDE and the speed rotator rate was modulated using MSR Rotator from PINE Instruments. GC RRDE were modified with COFs material by drop-casting 5 μL of the suspensions previously described. Hydrodynamic Lineal sweep voltammetry (LSV) were carried out in 0.1 M NaOH saturated with O_2 .

2.6. Theoretical Methods and Computational Details

Molecular fragments. In a first step, molecular fragments (NDA and TAPX) involved in the TAPX-NDI-COFs systems under study were computed within the framework of the density functional theory (DFT) using the Gaussian16 program.[55] It is well-known that calculation of molecular fragments provide important information about the molecular, electronic structure and

charge-transport properties of the formed of this kind of conjugated compounds.[50,56] To this end, two different hybrid functionals were used, such as the hybrid generalized gradient approximation (GGA) functional PBE0ra[57] and the long-range corrected hybrid functional CAM-B3LYP[58] together with the 6-31G**[59] and the cc-pVDZ[60] basis sets. All geometrical parameters were allowed to vary independently, and the calculated geometries were confirmed as minima by frequency calculations. Interestingly, PBE0 and CAM-B3LYP functionals, combined with the two different 6-31G** and cc-pVDZ basis sets predict an almost identical description of their molecular structural properties and topologies.

Periodic calculations. In a step forward, we used periodic boundary conditions to perform geometry optimization of a battery of stacked 3D layered TAPX-NDI-COFs models based on their canonical 2D network structures. For that purpose, the preliminary optimized building blocks can be considered as reasonable starting point geometries towards the assembling of the whole 2D network. Once the different models of the periodic system were constructed, they were fully optimized (simultaneous lattice/cell and structure optimizations) with the QUANTUM EXPRESSO plane-wave DFT code [61] Within this implementation, the GGA-PBE functional[62] was used to account for the exchange-correlation (XC) effects, at the same time that we use the Grimme DFT-D3 semi-empirical efficient vdW correction to include dispersion forces and energies in conventional DFT functionals.[63] Ultra-soft pseudopotentials have been used to model the ion-electron interaction within the H, C, N and O.[64,65] Brillouin zones have been sampled by means of optimal $[2 \times 2 \times 1]$ and $[2 \times 2 \times 8]$ Monkhorst-Pack grids[66] for the 2D layers and 3D crystals, respectively. One-electron wave-functions are expanded in a basis of plane-waves with a kinetic energy cutoff of 42 and 280 Ry for the kinetic energy and electronic density, respectively. The energy cutoff value has been exhaustively studied to achieve sufficient accuracy

to guarantee a full convergence in total energy and electronic density. As mentioned, we have performed simultaneous full lattice/cell and structure optimizations for the different canonical layered 3D system models. The atomic relaxations were carried out within a conjugate gradient minimization scheme until the maximum force acting on any atom was below $0.02 \text{ eV } \text{\AA}^{-1}$. Interlayer distances have been fully-relaxed following the aforementioned simultaneous lattice/structure relaxation protocol. The crystal-bulk models have been analyzed with several intermediate stacking-fashions between their both eclipsed (AA) and staggered (AB) configurations. Theoretical XRD simulations have been carried out by the MERCURY 3.10.3 program[67] on the most energetically stable crystal configurations obtained to make a direct comparison with the experimental evidence.

Topologies of valence and conduction bands. 3D isosurfaces of the orbital electronic densities corresponding to the valence and conduction electronic states of the different COF systems studied here ($\|\Psi_{\text{cond}}(\mathbf{r})\|^2$ and $\|\Psi_{\text{val}}(\mathbf{r})\|^2$) have been plotted by using the VMD 1.9.3 program (isosurface value of $0.0005 \text{ e}^- \text{\AA}^{-3}$).[68] From these figures we can extract information about the spatial localization and delocalization degree of these states, which may directly connect with the transport, catalytic and optical performance of the systems, the homogeneity in the spatial distribution of the states, as well as their orbital character to permit dipolar transitions between them.[69]

Photoabsorption spectra. The photoabsorption excitations of the molecular fragments representative of each COF-system (TAPB-NDI-a, TAPT-NDI-a and TAPA-NDI-a) have been calculated using time-dependent density functional theory (TDDFT),[70,71] implemented in GAUSSIAN16.[55] A treatment of the first order (linear) response of the system to the external electromagnetic field permits obtaining excitation energies and oscillator strengths from TD-DFT.

We have introduced an optimal number of unoccupied states in the basis to accurately obtain excitations with energies up to 5 eV (or, equivalently, above 250 nm), including singlet and triplet excitations. This requires including between 80 and 120 unoccupied single-particle states in the basis, depending on each specific cluster. Importantly, in order to achieve an improved description of the excitations within the TD-DFT we have used the long-range exchange-corrected functional CAM-B3LYP,[58] which includes a fraction (19%) of exact exchange at short range, very similar to the 20% fraction in the B3LYP, but tends to a limit of 65% of exact exchange at long range. CAM-B3LYP substantially improves the accuracy in the calculation of the excitations,[72] and appears to provide in some cases a similar accuracy compared to *ab initio* G_0W_0 and Bethe-Salpeter equation approaches.[73] It is interesting to remark that the similar short-range implementation of exchange-correlation used in B3LYP and CAM-B3LYP leads to the same ground-state geometries.

3. Results and discussion

3.1. Characterization

The formation of the imidized networks was confirmed by FTIR with the fading of the C=O anhydride and N-H amine bands, and with the emergence of the imide bands (Fig. 2A; Figs. S1-S3).[74,75] Thus, the bands at 1712 and 1665 cm^{-1} for TAPA-NDI-COF, 1715 and 1675 cm^{-1} for TAPB-NDI-COF and 1713 and 1671 cm^{-1} for TAPT-NDI-COF correspond to the symmetric and asymmetric stretching vibrations of the C=O group. The C-N-C imide stretching vibration appears at 1344 cm^{-1} for TAPA-NDI-COF, 1340 cm^{-1} for TAPB-NDI-COF and 1333 cm^{-1} for TAPT-NDI-COF.[50,76]

The solid state ^{13}C -CP/MAS-NMR spectra of NDI-based COFs (Fig. 2B.) show signals at 163.19 ppm for TAPA-NDI-COF, 164.35 ppm for TAPB-NDI-COF and 163.75 ppm for TAPT-NDI-COF

corresponding to the carbonyl carbons of the six-membered imide rings.[76] Two additional signals centered at 148.01 and 128.59 ppm for TAPA-NDI-COF, 143.3 and 129.5 ppm for TAPB-NDI-COF, and 138.05 and 130.16 ppm for TAPT-NDI-COF were assigned to the aromatic carbons from the naphthalene and phenyl moieties. Finally, the signal at 171.62 ppm of TAPT-NDI-COF was assigned to the triazine moiety.[76]

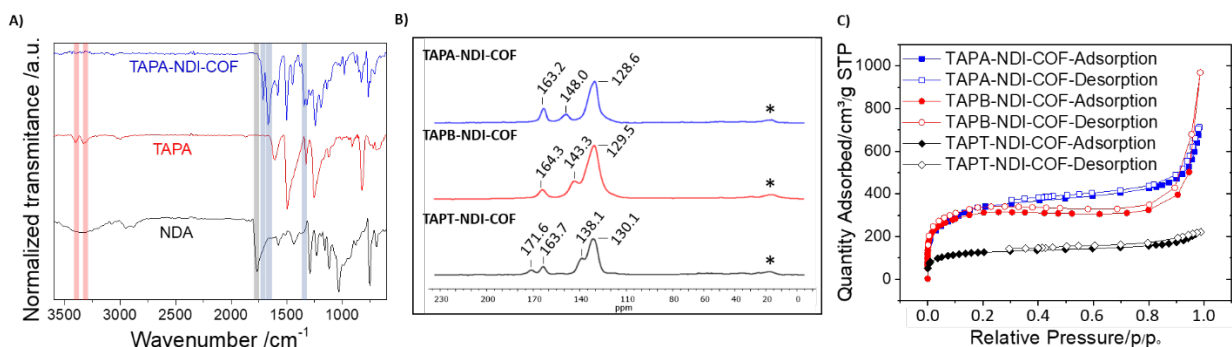


Figure 2. A) Comparison between the FTIR spectra of TAPA-NDI-COF (blue), TAPA (red) and NDA (black). B) ¹³C-CP/MAS-NMR spectra of TAPA-NDI-COF (blue), TAPB-NDI-COF (green) and TAPT-NDI-COF (red). Asterisks indicate spinning side bands. C) N₂ sorption isotherms for TAPA-NDI-COF (blue square), TAPB-NDI-COF (red circle) and TAPT-NDI-COF (black diamond).

Comparison between the FTIR and ¹³C-NMR spectra of the COFs and those of the molecular analogues allows to confirm the existence of an imidized network. The FTIR spectra of the networks are in agreement with those of the respective molecular analogues, showing the characteristic imide group stretching vibrations (Figs. S4-S6.). On the other hand, the ¹³C-NMR spectra of the molecular analogues fit well with the ¹³C-CP/MAS-NMR spectra of the respective networks (Figs. S7-S9).

The porosities of the TAPX-NDI-COFs were investigated by N₂ sorption isotherms at 77K (Fig. 2C.), from which a Brunauer-Emmett-Teller (BET) surface area of 1283 m²g⁻¹ was determined for TAPA-NDI-COF, 1138 m²g⁻¹ for TAPB-NDI-COF and 501 m²g⁻¹ for TAPT-NDI-COF. The pore volume at 0.95 p/p° of the COFs also decrease with the increase in the planarity of the trigonal node, being 0.839 cm³g⁻¹ for TAPA-NDI-COF, 0.777 cm³g⁻¹ for TAPB-NDI-COF and 0.596 cm³g⁻¹ for TAPT-NDI-COF. Finally, the pore size distribution calculated by non-local density functional theory (NLDFT) is centered at 2.3 nm for TAPA-NDI-COF, 2.6 nm for TAPB-NDI-COF and 2.6 nm for TAPT-NDI-COF which agrees with the expected values (Figs S10-S12).

The powder X-ray diffractions (PXRD) reveal the crystalline nature of the imide polymers. *In silico* experiments were performed using Gaussian16 and QUANTUM ESPRESSO software packages to solve the crystalline structure of the TAPX-NDI-COFs (Fig. 3; Figs S13-S15). Diffractograms corresponding to TAPB-NDI-COF and TAPT-NDI-COF show diffractions at 3.01°, 5.71° and 7.31°, corresponding to the (100), (200) and (210) facets while the diffractions observed for TAPA-NDI-COF appear at 3.35°, 6.5° and 8.62° as a consequence of its smaller pore size. The calculated face-to-face π - π stacking of TAPX-NDI-COFs reveal the decrease in the interlaminar spacing with the increasing planarity of the trigonal node, being 3.58 Å for TAPT-NDI-COF, 3.66 Å for TAPB-NDI-COF[50] and 3.67 Å for TAPA-NDI-COF. These values are smaller than that observed for efficiently packed linear conjugated polymers (3.7 Å[77]) and only slightly higher than those reported for graphite (3.4 Å[78]). Full width at half maximum (FWHM) analysis of the (100) diffraction maxima revealed some differences in the long-range ordering for TAPX-NDI-COFs. The FWHM values are 0.82 for TAPA-NDI-COF, 0.85 for TAPB-NDI-COF and 1.29 for TAPT-NDI-COF suggesting a lower crystallinity for TAPT-NDI-COF, which is in concordance with its lower surface area. We hypothesize that the differences in the nucleophilicity

of the triamine compound (TAPA>TAPB>TAPT) plays a crucial role during the networks curing, since the most activated triamine yields the most crystalline COF. In this way, it is worth pointing out that the use of an activated amine favours the production of more crystalline and porous architectures. In addition to the nucleophilicity of the C3 amine, due to the similar FWHM values of TAPA-NDI-COF and TAPB-NDI-COF we can envisage that the distortion of the trigonal knot also has a certain influence in the construction of more porous COFs through the increased interlaminar spacing and a subsequent incremented pore volume. Finally, due to the presence of a conjugation node at the imide positions, the electronic character of the trigonal knot should not produce any differences during the ORR experiments. In this way, we decided to continue our study to evaluate the oxygen electroreduction in presence of the TAPX-NDI-COFs in terms of their differences in porosity and interlaminar spacing as well as the NDI relative positions. Finally, thermal stabilities of the TAPX-NDI-COFs were tested by TGA (Fig. S16) revealing that the COF networks are stable up to 600°C.

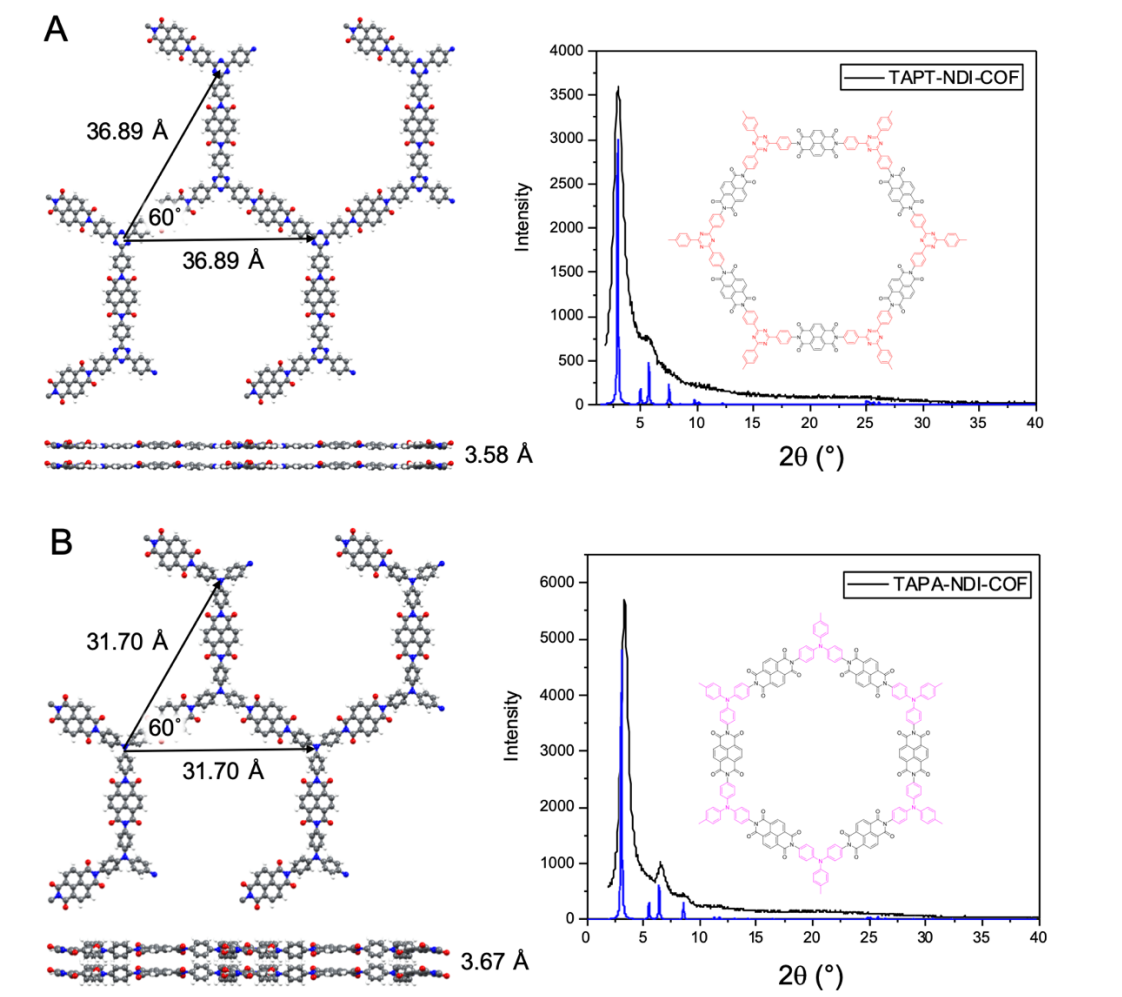


Figure 3. Top and side views of the computed DFT-optimized structures and simulated PXRD profiles (as compared with the experimental diffractograms) for the TAPT-NDI-COF (A) and TAPA-NDI-COF (B) in their most stable stacking configurations (AA in both cases). Most representative distances and angles are indicated for both COF-system structures.

To gain insight into the morphology of TAPX-NDI-COFs scanning electron microscopy (SEM) experiments were performed (Fig. 4), revealing a polygranular composition for all the crystalline polymers. This morphology seems to be favourable to properly exfoliate the COFs into covalent

organic nanosheets (CONs) and facilitate the dispersivity of the polymers as well as the interaction of the electrode with the electroactive NDI units during the catalysis experiments [79,80].

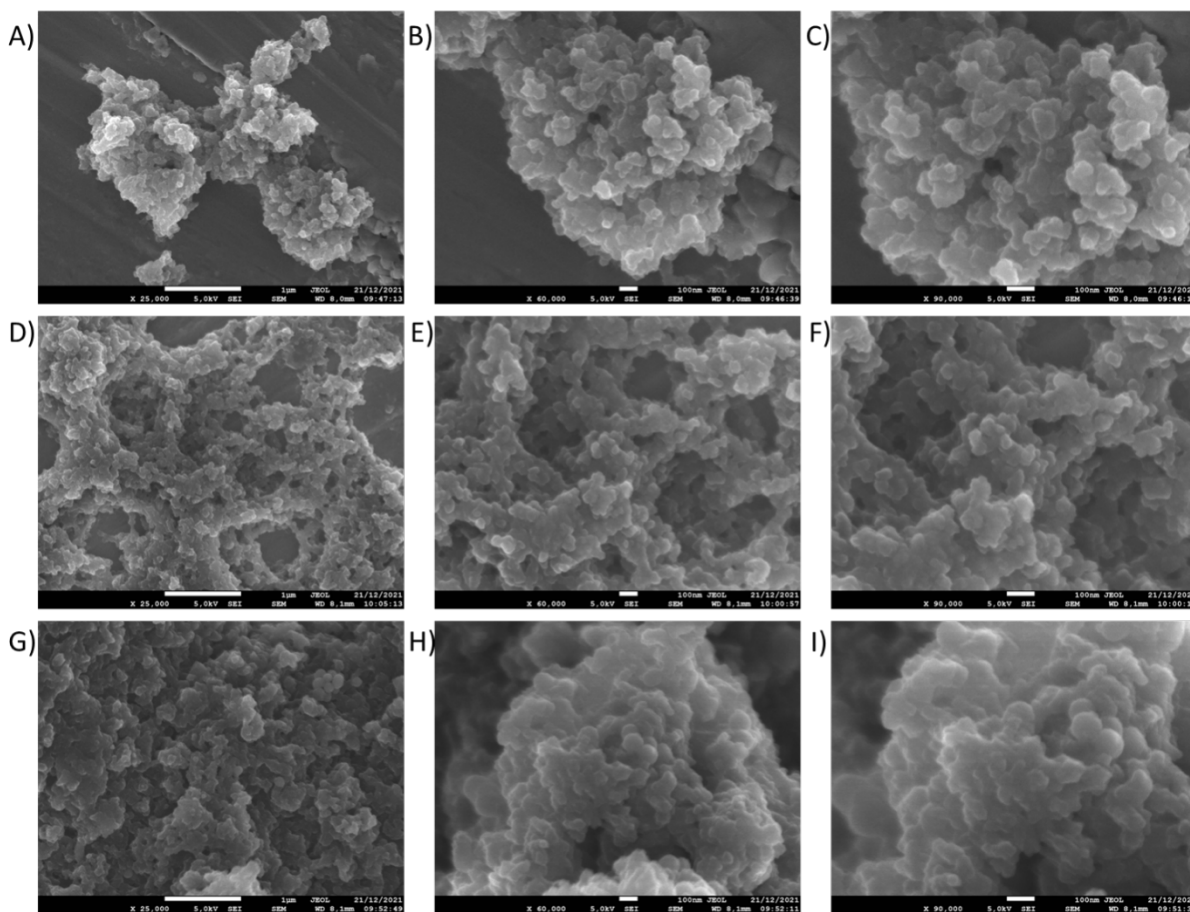


Figure 4. SEM micrographs of A) TAPA-NDI-COF 25.000x (scale bar 1µm), B) TAPA-NDI-COF 60.000x (scale bar 100 nm), C) TAPA-NDI-COF 90.000x (scale bar 100 nm), D) TAPB-NDI-COF 25.000x (scale bar 1µm), E) TAPB-NDI-COF 60.000x (scale bar 100 nm), F) TAPB-NDI-COF 90.000x (scale bar 100 nm), G) TAPT-NDI-COF 25.000x (scale bar 1µm), H) TAPT-NDI-COF 60.000x (scale bar 100 nm) and I) TAPT-NDI-COF 90.000x (scale bar 100 nm).

In this way, we performed liquid phase exfoliation (LPE) of the TAPX-NDI-COFs in an ultrasonic bath at 35 kHz for 30 minutes in an EtOH/H₂O (7/3) mixture (1 mg of COF/5 mL). Finally, ultracentrifugation at 6000 rpm for 15 minutes allowed to pull apart the non-exfoliated material affording CONs suspension. The colloidal nature of the delaminated COFs was

corroborated by Tyndall effect by appreciating the laser beam across the suspensions. Furthermore, the obtained CONs were investigated by SEM revealing a sheet-like morphology with less than approximately 50 nm thickness (Fig. 5A-C). Finally, transmission electronic microscopy (TEM) evidenced the thin layered CONs laminar structure (Fig. 5D-G).

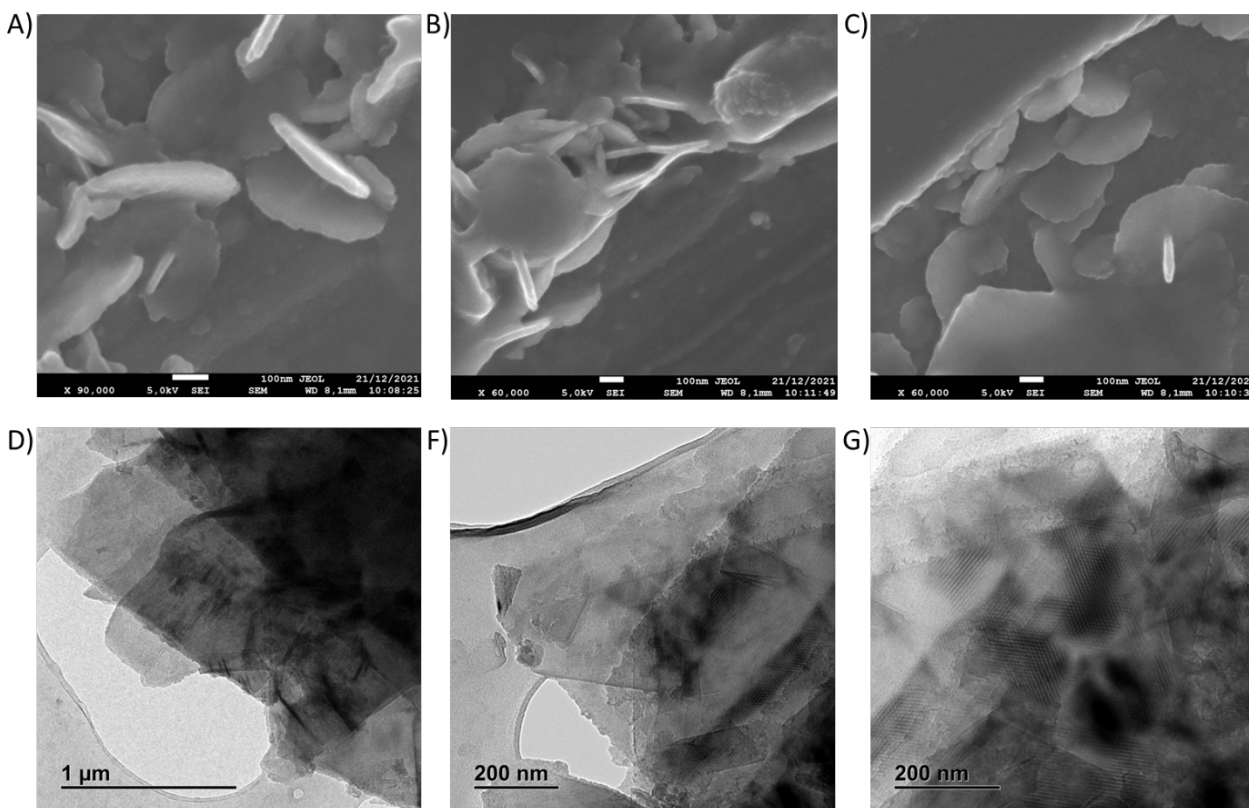


Figure 5. SEM micrographs of A) TAPA-NDI-CONs 90.000x (scale bar 100 nm), B) TAPN-NDI-CONs 90.000x (scale bar 100 nm) and C) TAPT-NDI-CONs 90.000x (scale bar 100 nm). TEM micrographs of D) TAPA-NDI-CONs, E) TAPB-NDI-CONs and F) TAPT-NDI-CONs.

3.2. Optical and electrochemical properties

To gain some insight into the optical properties of the TAPX-NDI-CONs, we have investigated their UV-vis absorption behavior. The characteristic absorption pattern of the naphthalenediimide moiety can be observed between 350 and 400 nm (Fig.6A) in the UV-vis absorption spectra of the exfoliated COFs.[38] The relative intensity of the (0,1) vibronic band with respect to the redshifted

(0,0) transition can be used as an indication for the presence of an efficient face-to-face π -type stacking of ryleneimide chromophores. Thus, strong vibronic coupling in the aggregates results in an enhanced (0,1) vibronic band compared to non-aggregated molecules. Therefore, upon aggregation of the NDI moieties, the ratio of the intensities of the (0,0) and the (0,1) transitions decreases and even can be inverted which is often used as an indication of aggregation[81-85] that can be rationalized by the molecular exciton model.[86-88] According to this, the most planar triazine derivative, TAPT-NDI-COF exhibit a significant aggregation with a (0,0)/(0,1) ratio of 0,95 which is inverted in comparison with that observed for the non-aggregated NDI-A model compound in chloroform solutions with a (0,0)/(0,1) ratio of 1.23. For the COF containing the less planar triarylamine derivative, TAPA-NDI-COF a (0,0)/(0,1) ratio of 1.06 is observed which is not very different to that of the non-aggregated NDI-A model compound. Finally, an intermediate situation is observed for the COF with the triphenylbenzene moiety with intermediate planarity for which a (0,0)/(0,1) ratio of 1.01 is observed.

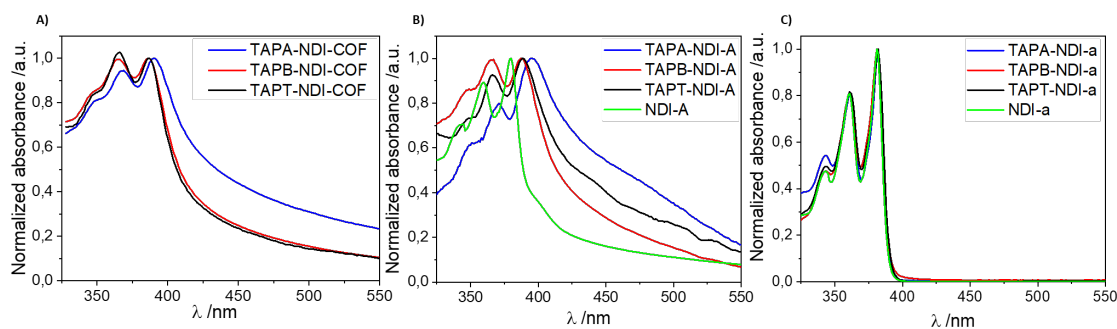


Figure 6. A) UV-vis absorption spectra of TAPX-NDI-COFs suspended in EtOH/H₂O (7/3), B) TAPX-NDI-A suspended in EtOH/H₂O (7/3) and C) TAPX-NDI-A solutions in CHCl₃.

The UV-vis absorption spectra of the monodisperse molecular analogues TAPX-NDI-A were measured for 10⁻⁵ M solutions in CHCl₃ and for EtOH/H₂O (7/3) suspensions (0.1 mg/mL) (Fig. 6B and 6C). The UV-vis absorption spectra of well dissolved TAPX-NDI-A molecules in

chloroform display the characteristic pattern of the non-aggregated NDI-A model compound with no modulation due to the different trigonal systems connected through the imide nitrogen atoms (Fig. 6C). This behavior agrees with the fact that NDI derivatives can be regarded as close chromophoric systems with an S₀-S₁ transition (polarized along the extended molecular axis) whose intensity and position remain unaltered by the respective imide substituents. Therefore, the imide (nitrogen) positions on NDI are nodes in the π -orbital molecular wavefunction, meaning that modification with different substitutions has a negligible influence on the electronic (light absorption and fluorescence) properties.[89]

Suspended TAPX-NDI-A analogues in EtOH/H₂O (7/3) mixtures show UV-vis absorption patterns that resemble that of the corresponding COFs, (Fig. 6B). It is worth pointing out that the absorption corresponding to the TAPX-NDI-A are bathochromically shifted in comparison with that of the NDI-A model compound. In order to analyze this behavior, it must be taken into account that that NDI core derivatives can be involved in aggregates through π - π interactions.[90-94]

To get an idea of the redox ability of the TAPX-NDI-COFs and the parent molecular analogues, TAPX-NDI-A, we have investigated their electrochemical behavior. We first analyzed the electrochemical behavior of the molecular analogues, with the aim of determining which groups are involved in the redox processes. The electrochemical measurements were carried out with the molecular analogues in solution, using chloroform as solvent and tetrabutylammonium perchlorate (TBAP) as supporting electrolyte. As expected, all models present two redox pairs at -0.70 V and -1.15 V (vs SCE), respectively, that are attributed to the NDI moiety reduction (Fig. 7A). The same processes are observed for NDI-A, confirming that the one-electron reduction processes observed are due to the NDI groups.[95] Only the TAPA-NDI-A presents a well-defined oxidation redox pair, which can be ascribed to the electrooxidation of TAPA groups. As it was expected, the NDI-

A does not present any oxidation process, as well as the other analogues (TAPT-NDI-A and TAPB-NDI-A), because of the higher potential required for the electrooxidation of TAPT and TAPB groups. The electrochemical behavior of the synthesized TAPX-NDI-COFs materials has also been studied in 0.1 M TBAP/CH₃Cl (Fig. 7B). GC electrodes were modified with TAPX-NDI-COF/Super P suspensions, and CV of the modified electrodes were obtained. The characteristic one-electron reduction process due to the NDI moiety is observed for the three COFs, with slightly differences, which indicates that the linking groups do not modify the electrochemical process. Similar results have been reported in the literature, showing the same behavior in covalent polymers.[96] Regarding the oxidation process, as it has been observed with the monodisperse molecular analogues, only TAPA-NDI-COF, the COF endowed with TAPA groups, presents a well-defined redox pair, associated with the oxidation of TAPA linkers in the COF network. Therefore, similarly to that observed for the NDI core, the electrochemical properties of TAPA are not affected by the insertion of this linker in the bi-dimensional covalent network.

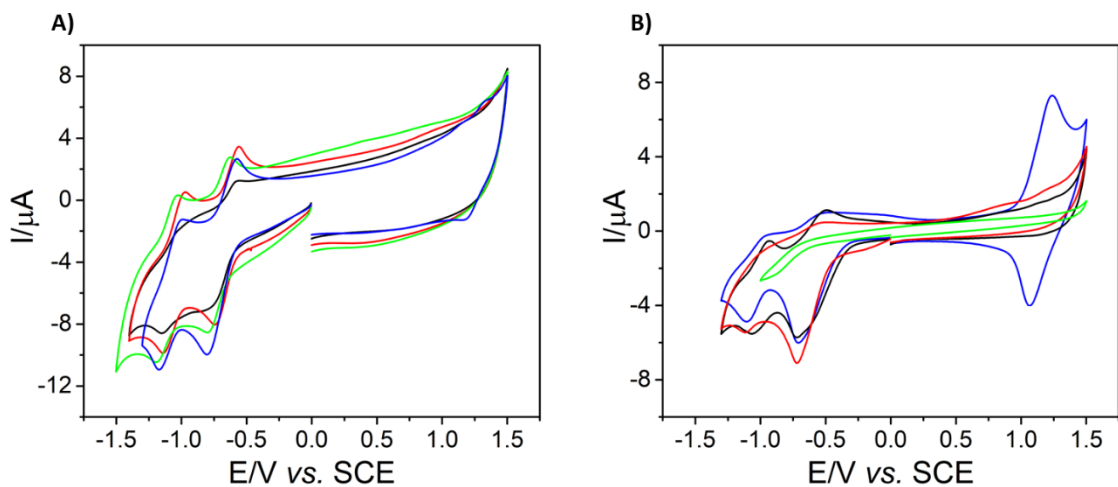


Figure 7. A) Cyclic voltammograms at a bare GC electrode in a 0.1 M tetrabutylammonium perchlorate /CHCl₃ solution containing 0.7 mM of TAPA-NDI-A (blue), TAPT-NDI-A (black), TAPB-NDI-A (red) and NDI-A (green) at 100 mV/s. B) Cyclic voltammograms at GC electrodes

modified with TAPA-NDI-COF-SuperP (blue), TAPT-NDI-COF-SuperP (black), TAPB-NDI-COF-SuperP (red) and SuperP (green) in a 0.1 M tetrabutylammonium perchlorate /CHCl₃ solution at 10 mV/s.

A large battery of DTF-based calculations has been carried out to rationalize the experimental data obtained from the UV-vis and electrochemical characterization. As stated above, substituents at the imide nitrogen have a negligible influence on the absorption properties of NDI derivatives because of the nodes of the HOMO and LUMO orbitals at the imide nitrogen atoms. This general behavior of the NDI derivatives can be observed also for the TAPX-NDI-COF and the parent monodisperse molecular analogues TAPX-NDI-A. In figure 8 are depicted the topologies of the valence and conduction bands of TAPX-NDI-COFs for which nodes can be observed at the imide nitrogen atoms. Furthermore, a spatial separation of the valence and conduction bands can be observed. Thus, the valence band is mainly located on the trigonal units while the conduction band is spread on the NDI units. As the conduction band is spread on the NDI units, which are identical in the three NDI-based COFs, the reduction potential of the three COFs is quite similar. On the other hand, as the valence band is located on the trigonal unit, different oxidation potentials may be expected for the three COFs. Thus, the stronger donor ability of the triarylamine moiety enables the detection of the oxidation potential of TAPA-NDI-COF while the oxidation process of the weaker electron donor benzene and triazine moieties in TAPB-NDI-COF and TAPT-NDI-COF respectively, lies at more positive potentials outside of the window of the electrochemical measurement and therefore cannot be detected.

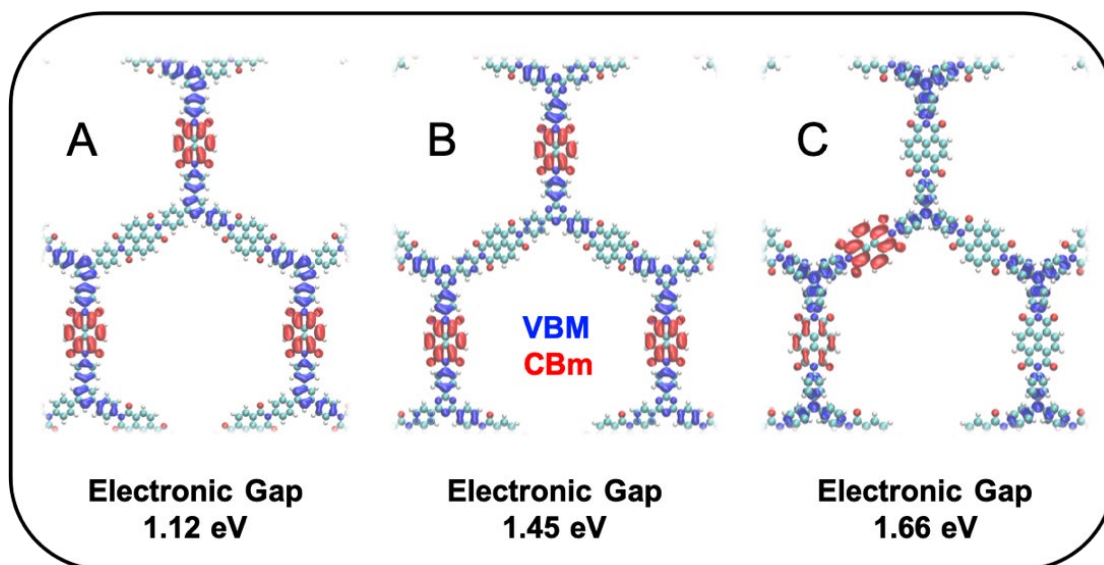


Figure 8. 3D isosurfaces (with values of $0.0005 \text{ e}^- \text{ \AA}^{-3}$ for sake of comparison) corresponding to the maximum of the valence band (VBM; blue) and minimum of the conduction band (CBm; red) for TAPB-NDI-COF (A), TAPT-NDI-COF (B) and TAPA-NDI-COF (C).

In addition, due to the particular topology of the valence and conduction band in TAPX-NDI-COFs and TAPX-NDI-As, their UV-vis absorption spectra are the mere superimposition of the absorption spectrum of the naphthalenediimide moiety at longer wavelengths and that of the trigonal subunits at shorter wavelengths. The slight differences observed in the UV-vis spectra of these systems are not due to any electronic communication between the naphthalenediimide moiety and the trigonal units.[81] The effect of the trigonal unit is mainly structural providing different tendency toward aggregation depending on their planarity.

This observation is further reinforced by the TDDFT-computed photoabsorption spectra obtained for the representative TAPB-NDI, TAPT-NDI and TAPA-NDI molecular units (Fig. S17) in EtOH/H₂O (7/3). The comparison with the experimental evidence is moderately good for that wavelength range. In the theoretical spectra we can observe two main peaks within the visible range located at around 350 and 400 nm, with the latest one more pronounced than the former, just

as in the experiment. It is important to notice that the three spectra are very similar, which reinforces the idea of a non-efficient communication between molecular moieties within the structure.

3.3. Electrocatalysis in the oxygen reduction reaction

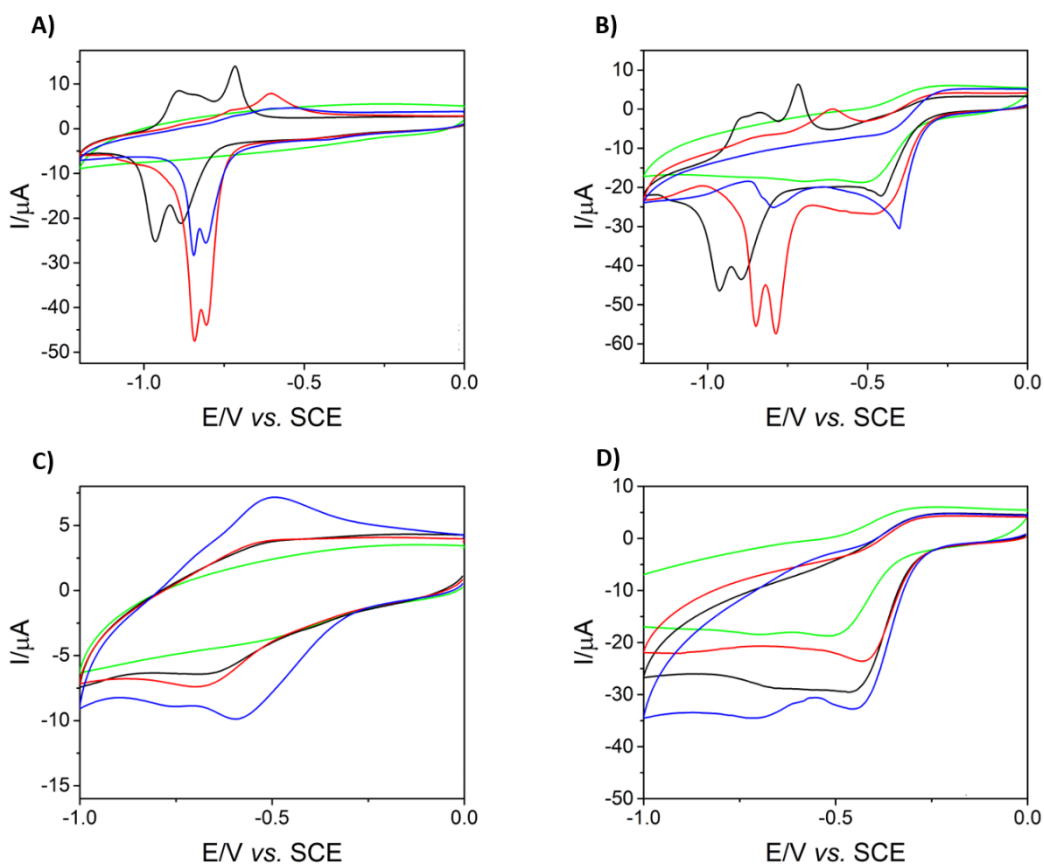


Figure 9. Cyclic voltammograms of GC electrodes modified with TAPA-NDI-A-SuperP (blue), TAPT-NDI-A-SuperP (black), TAPB-NDI-A-SuperP (red) and SuperP (green) in a 0.1 M NaOH solution in the absence A) and in the presence B) of O₂ at 10 mV/s. Cyclic voltammograms of GC electrodes modified with TAPA-NDI-COF-SuperP (blue), TAPT-NDI-COF-SuperP (black), TAPB-NDI-COF-SuperP (red) and SuperP (green) in a 0.1 M NaOH solution in the absence C) and in the presence D) of O₂ at 10 mV/s.

As we have recently shown that incorporating NDI as an electroactive building block makes the material energetically favorable to act as electrocatalyst towards the ORR,[50] we were intrigued about the suitability of using COFs with similar redox ability and different degrees of porosity and interlaminar spacing for electrocatalytic purposes. To analyze the capability of the NDI-based COFs as electrocatalysts in the oxygen reduction reaction (ORR), a preliminary study has been carried out with the monodisperse molecular analogues (Fig.9A and 9B). Glassy carbon (GC) electrodes were modified by drop-casting an aqueous suspension of the carbon conductor carbon Super P followed by the subsequent drop-casted deposition of solutions containing the NDI-based molecular analogues (TAPX-NDI-A). The electrochemical responses of these modified electrodes were studied in aqueous basic media (0.1 M NaOH), both in the absence and in the presence of molecular oxygen. In the absence of oxygen, the two processes ascribed to the electrochemical reduction of NDI in the TAPX-NDI-A molecular analogues (Fig. 9A), are now closer in basic medium. They appear at -0.80 and -0.84 V *vs.* SCE in the case of TAPA-NDI-A and TAPB-NDI-A, while in the case of TAPT-NDI-A the processes are shifted to -0.88 and -0.97 V *vs.* SCE. When molecular oxygen is present in solution (Fig. 9B), an electrocatalytic process is observed, even in the case of GC electrode only modified with Super P. There are not significant differences in the peaks ascribed to the NDI reduction in the case of molecular analogues, which suggest that the NDI cores are not involved in the ORR process in these analogues. Despite of this fact, a slight improvement of the onset potential can be observed when NDI molecular analogues are present in comparison with that observed for electrodes modified only with carbon-SuperP. This suggests that the NDI-based molecular analogues play a modest role in the ORR electrocatalysis.

Similar experiments were carried out using GC electrodes modified by drop-casting suspensions containing carbon SuperP and the NDI-based COFs. The electrochemical processes ascribed to the

NDI reduction in the absence of oxygen (Fig. 9C) appear at less negative potentials in comparison with those observed for their molecular analogues. This fact illustrates the role played by the incorporation of the NDI core in the COF networks to shift the reduction potential of the NDI-cores in the absence of oxygen. A similar shift to less negative potential scan be also observed during the ORR electroreduction using TAPX-NDI-COFs in the presence of oxygen (Fig. 9D). For all the electrodes modified with the NDI-based COFs, a *ca.* 50 mV shift is observed for the ORR onset potential in comparison with that observed for the GC electrode modified only with carbon SuperP. In addition, the current intensity improves when GC electrodes are modified with the TAPX-NDI-COF/carbon SuperP suspensions. Although the ORR onset potentials are quite similar for the three different NDI-based COFs under study, best results regarding current intensity are obtained for TAPA-NDI-COF. This behavior cannot be explained in terms of the influence of the trigonal substituents on the electron accepting ability of the naphthalimide moiety considering the negligible influence of the trigonal monomers in the redox ability of the naphthalimide moiety in the model molecular systems. As it was already mentioned, this behavior is characteristic of substituted ryleneimides due to the node in the π -molecular orbital at the imide (nitrogen) position on imide functionality. Thus, the better performance as electrocatalyst observed for TAPA-NDI-COF must be rationalized in terms of the different porosity observed for these COFs which can facilitate the access of oxygen to a larger amount of electroactive NDI moieties. In addition, it must be highlighted that the improvement on the electrocatalytic ability towards the ORR of the TAPX-NDI-COF networks in comparison with that observed for the parent molecular analogues (TAPX-NDI-A), confirms that the COFs' ordered structures play a key role in facilitating the electrochemical processes.

Additional Electrochemical impedance spectroscopy (EIS) experiments were carried out to characterize the electrocatalytic ORR process using TAPX-NDI-COF/carbon SuperP/GC electrodes (Fig. S18). According to the Nyquist plots, the modification of GC electrode with TAPX-NDI-COF decreases the resistance to ORR electron transfer, with TAPA-NDI-COF showing the smallest resistance followed by TAPB-NDI-COF and TAPT-NDI-COF. These results suggest that TAPA-NDI-COF would be the best electrocatalyst among the studied COF materials and agree well with those above described related to CV. As comparison GC electrode has also been modified with SuperP. Although a decrease of the resistance is also observed, it is smaller than in the case of TAPX-NDI-COFs.

The response to H_2O_2 has been studied by static cyclic voltammetry (Fig. S19). As can be observed, the electrocatalytic response to the electroreduction of H_2O_2 is moderate in the case of TAPT-NDI-COF and TAPA-NDI-COF but is high in the case of TAPB-NDI-COF. However, in the presence of O_2 there is almost not response to H_2O_2 for all TAPX-NDI-COFs. These results suggest that the presence of H_2O_2 barely affects the ORR electrocatalysis, confirming the high selectivity of TAPX-NDI-COF/carbon SuperP for O_2 electrocatalysis. Furthermore, this result also points out a good stability of TAPX-NDI-COF in the presence of high concentrations of H_2O_2 , which is interesting since H_2O_2 can be formed as a sub-product of the incomplete ORR through a two-electron mechanism.

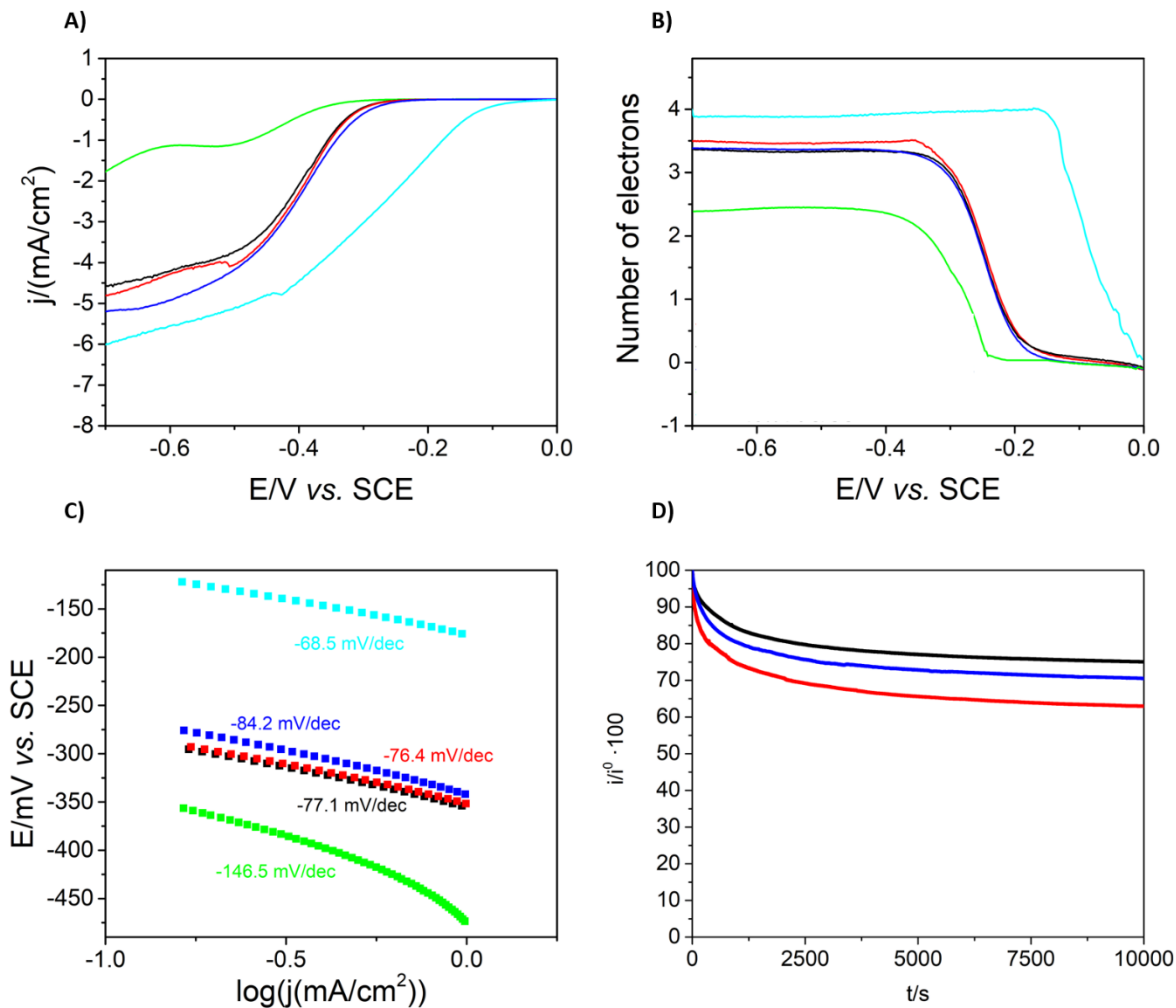


Figure 10. A) Hydrodynamic linear sweep voltammetry of GC electrode modified with TAPA-NDI-COF-SuperP (blue), TAPT-NDI-COF-SuperP (black), TAPB-NDI-COF-SuperP (red), 10% Pt-C (cyan) and SuperP (green) in a 0.1 M NaOH solution saturated with O₂ at 10 mV/s. B) Number of electrons exchanged in ORR at different potentials using RRDE of GC electrode modified with TAPA-NDI-COF-SuperP (blue), TAPT-NDI-COF-SuperP (black), TAPB-NDI-COF-SuperP (red), 10% Pt-C (cyan) and SuperP (green) in a 0.1 M NaOH solution saturated with O₂ at 10 mV/s. C) Tafel slope of ORR electrocatalysis obtain from results obtained with TAPA-NDI-COF-SuperP (blue), TAPT-NDI-COF-SuperP (black), TAPB-NDI-COF-SuperP (red), 10% Pt-C (cyan) and SuperP (green). D) Current intensity stability of TAPT-NDI-COF/carbon

SuperP/GC (black) TAPA-NDI-COF/carbon SuperP/GC (blue) and TAPB-NDI-COF/carbon SuperP/GC (red) electrodes operating in O₂ saturated 0.1 M NaOH solution at a constant potential (-0.4 V vs. SCE).

GC rotating disc-ring electrodes were modified with NDI-based COFs/Super P carbon or just Super P carbon, used as comparison, and employed to study the ORR in hydrodynamic conditions by lineal sweep voltammetry (Fig. 10A). A shift of the ORR onset potential of at least 66 mV is achieved using the electrodes modified with TAPB-NDI-COF and TAPT-NDI-COF. The improvement reaches 90 mV for the electrodes modified with TAPA-NDI-COF. It is also worth pointing out that the diffusional current increases when TAPX-NDI-COFs are used, exhibiting only small differences among the three different materials. Similarly, the TAPA-NDI-COF exhibits the best values of diffusion current according with that observed in the static CV experiments.

The number of electrons involved in the ORR can be calculated from equation (1):

$$(1) \ n = 4 \frac{i_D}{i_D + \frac{i_R}{N}}$$

Where n is the number of electrons, N is the collection efficiency of the ring (0.37 for the present geometrical arrangement) and i_D and i_R are the measured currents for the disk and ring electrodes, respectively. The number of electrons exchanged during the ORR have been plotted versus the potential applied (Fig. 10B). As can be seen, an important improvement in the number of electrons involved in the ORR process is observed, compared to the GC electrode modified only with superP carbon, where the number of electrons is close to 2.5, when the electrodes are modified with the TAPX-NDI-COF/SuperP. Indeed, in this case the number of electrons is near to 3.5, a value really close to the four-electron pathway desired for ORR electrocatalysts in fuel cell or air batteries applications. Tafel slopes have been obtained from the hydrodynamic sweep voltammograms of

GC electrodes modified with each TAPX-NDI-COF electrocatalyst, as well as Super P and 10% Pt-C as comparison (Fig. 10C). As one would expect, the lowest Tafel slope absolute value is obtained for the 10% Pt-C electrocatalyst (68.5 mV/dec). The Tafel slope absolute values obtained for TAPX-NDI-COF electrocatalysts are close to that obtained for platinum electrocatalyst (84.2-76.4 mV/dec), pointing out good ORR electrocatalyst features. A clear difference is observed with the value obtained for carbon SuperP electrocatalyst (146.5 mV/dec), being a clear evidence of the role of the TAPX-NDI-COF materials in the ORR electrocatalyzed process.

The stability of the TAPX-NDI-COF electrocatalysts during ORR has been tested applying a fixed potential of -0.4 V vs. SCE for 10k seconds in hydrodynamic conditions in an O₂ saturated 0.1 M NaOH solution (Fig. 10D). The best stability was obtained for TAPT-NDI-COF, keeping 75 % of the initial current after 10k seconds of ORR electrocatalysis operation. TAPA-NDI-COF and TAPB-NDI-COF kept 71 % and 63 % of the initial current, respectively.

In a proof-of-concept attempt to propose a viable ORR mechanism for these systems, we have studied the intermediate ORR steps and the associated free energies, in a first approximation, within the representative NDI molecule after its chemically well-known two-electron reduction (Fig. 11A). After this reduction, we have detected different active sites to develop the reaction. Nonetheless, the one able to complete the full reaction is the C atom linked to the O atoms (Fig. 11B). Attempts to anchor the functional groups involved in the ORR on other molecular sites finished with them, after full relaxation, linking to the previously mentioned C atom. Gibbs free energy diagram has been constructed for the site in Fig. 11C in the two-electron reduced NDI molecule according to the formalism shown in [97] (Fig. 11C) at standard conditions (pH=0, T=298.15 K). Since the barriers between the intermediates are not included, the free energy diagram represents a first step towards the complete picture of the reaction path. The effect of

liquid water was implicitly considered as we used liquid water as reference. However, the interaction of water with the intermediates at the surfaces has been neglected. Results predict a theoretical overpotential controlling the reaction in this model system of 1.12 eV coming from the first step of the reaction. Interestingly, this metal-free COF-system shows an overpotential value and a free energy diagram trend similar to many transition-metal La-perovskites analyzed in detail in previous literature,[97] which theoretically justifies a moderate ORR catalytic performance.

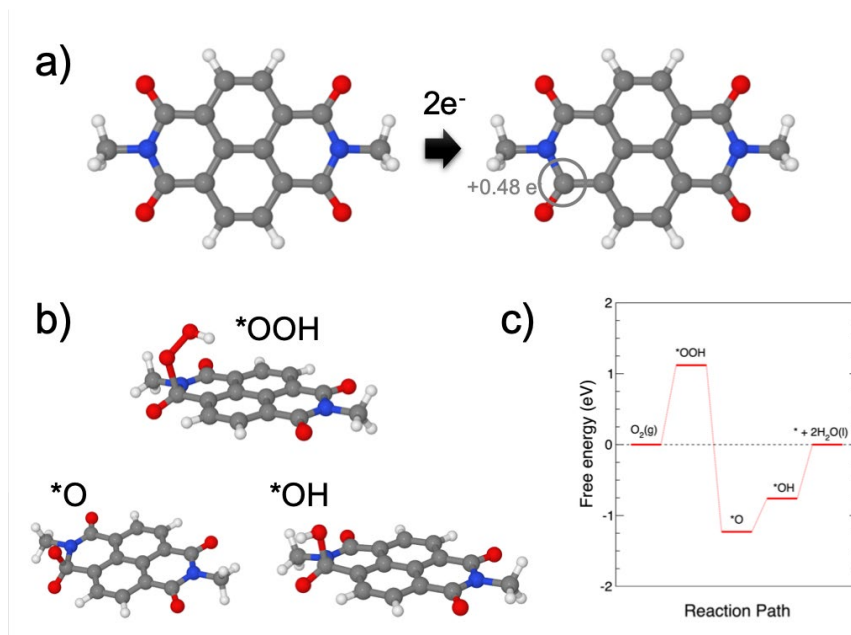


Figure 11. A) 2e⁻ reduction of the in the NDI molecule. B) Optimized intermediate ORR steps: *OOH, *O and *OH adsorption in the most active C-site able to develop the full ORR reaction. C) Gibbs free energy diagram for the ORR mechanism.

4. Summary and Conclusions

In summary, we have developed a family of hexagonal 2D imide-based COFs containing electroactive naphthalenediimide (NDI) units that promotes the formation of face-to-face π - π stacked structures with intrinsic porosity and large surface areas. Different suitably functionalized trigonal systems have been used to constitute the nodes of the hexagonal networks and theoretical

calculations carried out to solve the crystalline structures of the TAPX-NDI-COFs reveal a decrease in the interlaminar spacing with the increasing planarity of the trigonal nodes. The three COFs have similar reduction potentials due to the lack of electronic communication between the electroactive naphthalenediimide moieties and the trigonal linkers. Therefore, the followed strategy offers the possibility of obtaining electroactive COFs with similar redox ability but different degrees of porosity and interlaminar spacing.

These non-metalated pristine COFs have been tested as electrocatalysts in the oxygen reduction reaction without the need of an additional pyrolysis step. It has been determined that 3.5 electrons are exchanged during the ORR, a value close to the 4-electron pathway desired for ORR electrocatalysts in fuel cells. It must be highlighted that the electrocatalytic ability towards the ORR of the TAPX-NDI-COF networks is significantly higher in comparison with that observed for parent molecular models (TAPX-NDI-A), showing that the COFs' ordered structures play a key role in facilitating the electrochemical processes. Furthermore, more efficient electrocatalysis is observed for the more porous COF due to the easier access of oxygen to larger amounts of electroactive NDI catalytic centers.

Our work reveals that the incorporation of electroactive naphthalenediimide moieties into a COF is an efficient strategy to develop organic materials with ORR electrocatalytic activity. The fact that interlaminar spacing and porosity play a key role on the ORR catalytic activity provides valuable insights in order to improve the ORR catalytic activity of such electroactive COF-based materials. In fact, the COF-based ORR electrocatalysts described in this work compare well with other previously described metal-free COFs prepared without pyrolysis (table S2). Although for real applications these materials offer performances are far from those offered by metal based electrocatalysts, the results showed in this work point out the relevance of layer stacking, showing

a great difference between COFs containing the same electroactive moiety but different linker units that modify their layer stacking. This study opens a great variety of possibilities for future research, giving evidences of the great relevance of choosing both, electroactive groups with good electrocatalytic activity as well as the most suitable linker moieties allowing the arrangement of the electroactive centres in the most favourable disposition for electrocatalysis.

Appendix. A. Supplementary data.

Supplementary data to this article can be found online at:

Author Contributions

The manuscript was written through contributions of all authors. All authors have given approval to the final version of the manuscript.‡ These authors contributed equally.

Funding Sources

MICINN (PID2019-106268GB-C33;RED2018-102412-T; PID2020-116728RB-I00). UCM (INV.GR.00.1819.10759). Comunidad de Madrid (P2018/NMT-4349 TRANSNANOAVANSENS Program; SI3/PJI/2021-00341)

Declaration of Competing Interest

The authors declare that they have no known competing financial interests or personal relationships that could have appeared to influence the work reported in this paper.

Data availability

The data is available upon request from the corresponding authors

Acknowledgements

This work was financially supported by MICINN (PID2019-106268GB-C33; RED2018-102412-T; PID2020-116728RB-I00), Comunidad de Madrid (P2018/NMT-4349 TRANSNANOAVANSENS Program; SI3/PJI/2021-00341) and the UCM (INV.GR.00.1819.10759). MMF acknowledges Comunidad de Madrid for a predoctoral contract, CNME for the TEM and SEM images and Álvaro Fuentes Benavides for the art-work of this article.

References

1. Ma, R., Lin, G., Zhou, Y., Liu, Q., Zhang, T., Shan, G., Yang, M., Wang, J., *npj Computational Materials* (2019) **5** (1), 78 10.1038/s41524-019-0210-3
2. Zhou, Y., Chen, G., Zhang, J., *Journal of Materials Chemistry A* (2020) **8** (40), 20849 10.1039/D0TA07900F
3. Bajracharya, S., ElMekawy, A., Srikanth, S., Pant, D., 6 - Cathodes for microbial fuel cells. In *Microbial Electrochemical and Fuel Cells*, Scott, K., and Yu, E. H., (eds.) Woodhead Publishing, Boston, (2016), pp 179 <https://doi.org/10.1016/B978-1-78242-375-1.00006-X>
4. Wang, N., Ma, S., Zuo, P., Duan, J., Hou, B., *Advanced Science* **n/a** (n/a), 2100076 <https://doi.org/10.1002/advs.202100076>
5. Debe, M. K., *Nature* (2012) **486** (7401), 43 10.1038/nature11115
6. Alaswad, A., Palumbo, A., Dassisti, M., Olabi, A. G., Fuel Cell Technologies, Applications, and State of the Art. A Reference Guide. In *Reference Module in Materials Science and Materials Engineering*, Elsevier(2016)<https://doi.org/10.1016/B978-0-12-803581-8.04009-1>
7. Jaouen, F., Proietti, E., Lefèvre, M., Chenitz, R., Dodelet, J.-P., Wu, G., Chung, H. T., Johnston, C. M., Zelenay, P., *Energy & Environmental Science* (2011) **4** (1), 114 10.1039/C0EE00011F
8. Morozan, A., Jusselme, B., Palacin, S., *Energy & Environmental Science* (2011) **4** (4), 1238 10.1039/C0EE00601G
9. Zhu, Y., Zhou, W., Yu, J., Chen, Y., Liu, M., Shao, Z., *Chemistry of Materials* (2016) **28** (6), 1691 10.1021/acs.chemmater.5b04457
10. Parra-Puerto, A., Ng, K. L., Fahy, K., Goode, A. E., Ryan, M. P., Kucernak, A., *ACS Catalysis* (2019) **9** (12), 11515 10.1021/acscatal.9b03359
11. Chen, G., Wan, H., Ma, W., Zhang, N., Cao, Y., Liu, X., Wang, J., Ma, R., *Advanced Energy Materials* (2020) **10** (11), 1902535 <https://doi.org/10.1002/aenm.201902535>
12. Browne, M. P., Sofer, Z., Pumera, M., *Energy & Environmental Science* (2019) **12** (1), 41 10.1039/C8EE02495B
13. Tang, H., Karnaushenko, D. D., Neu, V., Gabler, F., Wang, S., Liu, L., Li, Y., Wang, J., Zhu, M., Schmidt, O. G., *Small* (2020) **16** (35), 2002410 <https://doi.org/10.1002/smll.202002410>
14. Liu, M., Zhao, Z., Duan, X., Huang, Y., *Advanced Materials* (2019) **31** (6), 1802234 <https://doi.org/10.1002/adma.201802234>

15. Raj, C. R., Samanta, A., Noh, S. H., Mondal, S., Okajima, T., Ohsaka, T., *Journal of Materials Chemistry A* (2016) **4** (29), 11156 10.1039/C6TA03300H
16. Hu, Z., Guo, Z., Zhang, Z., Dou, M., Wang, F., *ACS Applied Materials & Interfaces* (2018) **10** (15), 12651 10.1021/acsami.8b00512
17. Jiang, K., Back, S., Akey, A. J., Xia, C., Hu, Y., Liang, W., Schaak, D., Stavitski, E., Nørskov, J. K., Siahrostami, S., Wang, H., *Nature Communications* (2019) **10** (1), 3997 10.1038/s41467-019-11992-2
18. Martínez-Periñán, E., Bravo, I., Rowley-Neale, S. J., Lorenzo, E., Banks, C. E., *Electroanalysis* (2018) **30** (3), 436 <https://doi.org/10.1002/elan.201700718>
19. Yan, X., Jia, Y., Odedairo, T., Zhao, X., Jin, Z., Zhu, Z., Yao, X., *Chemical Communications* (2016) **52** (52), 8156 10.1039/C6CC03687B
20. Tang, C., Wang, H.-F., Chen, X., Li, B.-Q., Hou, T.-Z., Zhang, B., Zhang, Q., Titirici, M.-M., Wei, F., *Advanced Materials* (2016) **28** (32), 6845 <https://doi.org/10.1002/adma.201601406>
21. Jia, Y., Chen, J., Yao, X., *Materials Chemistry Frontiers* (2018) **2** (7), 1250 10.1039/C8QM00070K
22. Yan, X., Jia, Y., Yao, X., *Chemical Society Reviews* (2018) **47** (20), 7628 10.1039/C7CS00690J
23. Peng, P., Zhou, Z., Guo, J., Xiang, Z., *ACS Energy Letters* (2017) **2** (6), 1308 10.1021/acsenenergylett.7b00267
24. Lin, C.-Y., Zhang, D., Zhao, Z., Xia, Z., *Advanced Materials* (2018) **30** (5), 1703646 <https://doi.org/10.1002/adma.201703646>
25. Roy, S., Bandyopadhyay, A., Das, M., Ray, P. P., Pati, S. K., Maji, T. K., *Journal of Materials Chemistry A* (2018) **6** (14), 5587 10.1039/C8TA00099A
26. Guo, J., Lin, C.-Y., Xia, Z., Xiang, Z., *Angewandte Chemie International Edition* (2018) **57** (38), 12567 <https://doi.org/10.1002/anie.201808226>
27. Long, X., Li, D., Wang, B., Jiang, Z., Xu, W., Wang, B., Yang, D., Xia, Y., *Angewandte Chemie International Edition* (2019) **58** (33), 11369 <https://doi.org/10.1002/anie.201905468>
28. Jia, N., Yang, T., Shi, S., Chen, X., An, Z., Chen, Y., Yin, S., Chen, P., *ACS Sustainable Chemistry & Engineering* (2020) **8** (7), 2883 10.1021/acssuschemeng.9b07047
29. Wang, N., Ma, S., Zuo, P., Duan, J., Hou, B., *Advanced Science* (2021) **n/a** (n/a), 2100076 <https://doi.org/10.1002/advs.202100076>
30. Wu, Z.-Y., Xu, X.-X., Hu, B.-C., Liang, H.-W., Lin, Y., Chen, L.-F., Yu, S.-H., *Angewandte Chemie International Edition* (2015) **54** (28), 8179 <https://doi.org/10.1002/anie.201502173>
31. Côté, A. P., Benin, A. I., Ockwig, N. W., O'Keeffe, M., Matzger, A. J., Yaghi, O. M., *Science* (2005) **310** (5751), 1166 10.1126/science.1120411
32. Geng, K., He, T., Liu, R., Dalapati, S., Tan, K. T., Li, Z., Tao, S., Gong, Y., Jiang, Q., Jiang, D., *Chemical Reviews* (2020) **120** (16), 8814 10.1021/acs.chemrev.9b00550
33. Segura, J. L., Mancheño, M. J., Zamora, F., *Chemical Society Reviews* (2016) **45** (20), 5635 10.1039/C5CS00878F
34. Spitler, E. L., Colson, J. W., Uribe-Romo, F. J., Woll, A. R., Giovino, M. R., Saldivar, A., Dichtel, W. R., *Angewandte Chemie International Edition* (2012) **51** (11), 2623 <https://doi.org/10.1002/anie.201107070>
35. Nagai, A., Guo, Z., Feng, X., Jin, S., Chen, X., Ding, X., Jiang, D., *Nature Communications* (2011) **2** (1), 536 10.1038/ncomms1542

36. Zhang, H., Zhu, M., Schmidt, O. G., Chen, S., Zhang, K., *Advanced Energy and Sustainability Research* (2021) **2** (4), 2000090 <https://doi.org/10.1002/aesr.202000090>
37. Bhunia, S., Das, S. K., Jana, R., Peter, S. C., Bhattacharya, S., Addicoat, M., Bhaumik, A., Pradhan, A., *ACS Applied Materials & Interfaces* (2017) **9** (28), 23843 10.1021/acsami.7b06968
38. Dusold, C., Platzer, B., Haines, P., Reger, D., Jux, N., Guldi, D. M., Hirsch, A., *Chemistry – A European Journal* (2021) **27** (5), 1670 <https://doi.org/10.1002/chem.202004273>
39. Gao, Z., Yu, Z., Huang, Y., He, X., Su, X., Xiao, L., Yu, Y., Huang, X., Luo, F., *Journal of Materials Chemistry A* (2020) **8** (12), 5907 10.1039/C9TA14023A
40. Hijazi, I., Bourgeteau, T., Cornut, R., Moroza, A., Filoramo, A., Leroy, J., Derycke, V., Jousseme, B., Campidelli, S., *Journal of the American Chemical Society* (2014) **136** (17), 6348 10.1021/ja500984k
41. Zuo, Q., Cheng, G., Luo, W., *Dalton Transactions* (2017) **46** (29), 9344 10.1039/C7DT01694H
42. Li, Q., Shao, Q., Wu, Q., Duan, Q., Li, Y., Wang, H.-g., *Catalysis Science & Technology* (2018) **8** (14), 3572 10.1039/C8CY00483H
43. Xiang, Z., Cao, D., Huang, L., Shui, J., Wang, M., Dai, L., *Advanced Materials* (2014) **26** (20), 3315 <https://doi.org/10.1002/adma.201306328>
44. Briega-Martos, V., Ferre-Vilaplana, A., de la Peña, A., Segura, J. L., Zamora, F., Feliu, J. M., Herrero, E., *ACS Catalysis* (2017) **7** (2), 1015 10.1021/acscatal.6b03043
45. Pachfule, P., Dhavale, V. M., Kandambeth, S., Kurungot, S., Banerjee, R., *Chemistry – A European Journal* (2013) **19** (3), 974 <https://doi.org/10.1002/chem.201202940>
46. Li, D., Jia, Y., Chang, G., Chen, J., Liu, H., Wang, J., Hu, Y., Xia, Y., Yang, D., Yao, X., *Chem* (2018) **4** (10), 2345 <https://doi.org/10.1016/j.chempr.2018.07.005>
47. Xu, Q., Tang, Y., Zhang, X., Oshima, Y., Chen, Q., Jiang, D., *Advanced Materials* (2018) **30** (15), 1706330 <https://doi.org/10.1002/adma.201706330>
48. Wu, S., Li, M., Phan, H., Wang, D., Herng, T. S., Ding, J., Lu, Z., Wu, J., *Angewandte Chemie International Edition* (2018) **57** (27), 8007 <https://doi.org/10.1002/anie.201801998>
49. Kong, L., Zhong, M., Shuang, W., Xu, Y., Bu, X.-H., *Chemical Society Reviews* (2020) **49** (8), 2378 10.1039/C9CS00880B
50. Royuela, S., Martínez-Periñán, E., Arrieta, M. P., Martínez, J. I., Ramos, M. M., Zamora, F., Lorenzo, E., Segura, J. L., *Chemical Communications* (2020) **56** (8), 1267 10.1039/C9CC06479F
51. Lv, J., Tan, Y.-X., Xie, J., Yang, R., Yu, M., Sun, S., Li, M.-D., Yuan, D., Wang, Y., *Angewandte Chemie International Edition* (2018) **57** (39), 12716 <https://doi.org/10.1002/anie.201806596>
52. Steyrleuthner, R., Di Pietro, R., Collins, B. A., Polzer, F., Himmelberger, S., Schubert, M., Chen, Z., Zhang, S., Salleo, A., Ade, H., Facchetti, A., Neher, D., *Journal of the American Chemical Society* (2014) **136** (11), 4245 10.1021/ja4118736
53. Morandeira, A., Fortage, J., Edvinsson, T., Le Pleux, L., Blart, E., Boschloo, G., Hagfeldt, A., Hammarström, L., Odobel, F., *The Journal of Physical Chemistry C* (2008) **112** (5), 1721 10.1021/jp077446n
54. Aster, A., Rumble, C., Bornhof, A.-B., Huang, H.-H., Sakai, N., Šolomek, T., Matile, S., Vauthey, E., *Chemical Science* (2021) **12** (13), 4908 10.1039/D1SC00285F
55. Frisch, M. J., Trucks, G. W., Schlegel, H. B., Scuseria, G. E., Robb, M. A., Cheeseman, J. R., Scalmani, G., Barone, V., Petersson, G. A., Nakatsuji, H., Li, X., Caricato, M., Marenich,

- A. V., Bloino, J., Janesko, B. G., Gomperts, R., Mennucci, B., Hratchian, H. P., Ortiz, J. V., Izmaylov, A. F., Sonnenberg, J. L., Williams, Ding, F., Lipparini, F., Egidi, F., Goings, J., Peng, B., Petrone, A., Henderson, T., Ranasinghe, D., Zakrzewski, V. G., Gao, J., Rega, N., Zheng, G., Liang, W., Hada, M., Ehara, M., Toyota, K., Fukuda, R., Hasegawa, J., Ishida, M., Nakajima, T., Honda, Y., Kitao, O., Nakai, H., Vreven, T., Throssell, K., Montgomery Jr., J. A., Peralta, J. E., Ogliaro, F., Bearpark, M. J., Heyd, J. J., Brothers, E. N., Kudin, K. N., Staroverov, V. N., Keith, T. A., Kobayashi, R., Normand, J., Raghavachari, K., Rendell, A. P., Burant, J. C., Iyengar, S. S., Tomasi, J., Cossi, M., Millam, J. M., Klene, M., Adamo, C., Cammi, R., Ochterski, J. W., Martin, R. L., Morokuma, K., Farkas, O., Foresman, J. B., Fox, D. J., Gaussian 16 Rev. C.01. Wallingford, CT, (2016)
56. Albacete, P., Martínez, J. I., Li, X., López-Moreno, A., Mena-Hernando, S. a., Platero-Prats, A. E., Montoro, C., Loh, K. P., Pérez, E. M., Zamora, F., *Journal of the American Chemical Society* (2018) **140** (40), 12922 10.1021/jacs.8b07450
 57. Perdew, J. P., Ernzerhof, M., Burke, K., *The Journal of Chemical Physics* (1996) **105** (22), 9982 10.1063/1.472933
 58. Yanai, T., Tew, D. P., Handy, N. C., *Chemical Physics Letters* (2004) **393** (1), 51 <https://doi.org/10.1016/j.cplett.2004.06.011>
 59. Hehre, W. J., Ditchfield, R., Pople, J. A., *The Journal of Chemical Physics* (1972) **56** (5), 2257 10.1063/1.1677527
 60. Dunning, T. H., *The Journal of Chemical Physics* (1989) **90** (2), 1007 10.1063/1.456153
 61. Giannozzi, P., Baroni, S., Bonini, N., Calandra, M., Car, R., Cavazzoni, C., Ceresoli, D., Chiarotti, G. L., Cococcioni, M., Dabo, I., Dal Corso, A., de Gironcoli, S., Fabris, S., Fratesi, G., Gebauer, R., Gerstmann, U., Gougoussis, C., Kokalj, A., Lazzeri, M., Martin-Samos, L., Marzari, N., Mauri, F., Mazzarello, R., Paolini, S., Pasquarello, A., Paulatto, L., Sbraccia, C., Scandolo, S., Sclauzero, G., Seitsonen, A. P., Smogunov, A., Umari, P., Wentzcovitch, R. M., *J Phys Condens Matter* (2009) **21** (39), 395502 10.1088/0953-8984/21/39/395502
 62. Perdew, J. P., Burke, K., Ernzerhof, M., *Physical Review Letters* (1996) **77** (18), 3865 10.1103/PhysRevLett.77.3865
 63. Grimme, S., *Journal of Computational Chemistry* (2006) **27** (15), 1787 <https://doi.org/10.1002/jcc.20495>
 64. Rappe, A. M., Rabe, K. M., Kaxiras, E., Joannopoulos, J. D., *Physical Review B* (1990) **41** (2), 1227 10.1103/PhysRevB.41.1227
 65. Mounet, N., and Marzari, N., *Physical Review B* (2005) **71** (20), 205214 10.1103/PhysRevB.71.205214
 66. Pack, J. D., and Monkhorst, H. J., *Physical Review B* (1977) **16** (4), 1748 10.1103/PhysRevB.16.1748
 67. Macrae, C. F., Sovago, I., Cottrell, S. J., Galek, P. T. A., McCabe, P., Pidcock, E., Platings, M., Shields, G. P., Stevens, J. S., Towler, M., Wood, P. A., Mercury 4.0: from visualization to analysis, design and prediction. In *J Appl Crystallogr*, (2020), Vol. 53, pp 226 10.1107/s1600576719014092
 68. Humphrey, W., Dalke, A., Schulten, K., *Journal of Molecular Graphics* (1996) **14** (1), 33 [https://doi.org/10.1016/0263-7855\(96\)00018-5](https://doi.org/10.1016/0263-7855(96)00018-5)
 69. Gámez-Valenzuela, S., Echeverri, M., Gómez-Lor, B., Martínez, J. I., Ruiz Delgado, M. C., *Journal of Materials Chemistry C* (2020) **8** (43), 15416 10.1039/D0TC03139A
 70. Rubio, A., Balbás, L. C., Alonso, J. A., *Phys Rev B Condens Matter* (1992) **45** (23), 13657 10.1103/physrevb.45.13657

71. CASIDA, M. E., Time-Dependent Density Functional Response Theory for Molecules. In *Recent Advances in Density Functional Methods*, pp 155 10.1142/9789812830586_0005
72. Bourass, M., Touimi Benjelloun, A., Benzakour, M., Mcharfi, M., Hamidi, M., Bouzzine, S. M., Serein Spirau, F., Jarroson, T., Lere-Porte, J. P., Sotiropoulos, J.-M., Bouachrine, M., *Journal of Materials and Environmental Science* (2015) **6** (6), 1542
73. Wilhelm, J., Del Ben, M., Hutter, J., *Journal of Chemical Theory and Computation* (2016) **12** (8), 3623 10.1021/acs.jctc.6b00380
74. Jiang, L., Tian, Y., Sun, T., Zhu, Y., Ren, H., Zou, X., Ma, Y., Meihaus, K. R., Long, J. R., Zhu, G., *J Am Chem Soc* (2018) **140** (46), 15724 10.1021/jacs.8b08174
75. Wang, G., Chandrasekhar, N., Biswal, B. P., Becker, D., Paasch, S., Brunner, E., Addicoat, M., Yu, M., Berger, R., Feng, X., *Adv Mater* (2019) **31** (28), e1901478 10.1002/adma.201901478
76. Liebl, M. R., and Senker, J., *Chemistry of Materials* (2013) **25** (6), 970 10.1021/cm4000894
77. Liu, Y., Liu, Y., Zhan, X., *Macromolecular Chemistry and Physics* (2011) **212** (5), 428 <https://doi.org/10.1002/macp.201000677>
78. Berashevich, J., and Chakraborty, T., *The Journal of Physical Chemistry C* (2011) **115** (50), 24666 10.1021/jp2095032
79. Burke, D. W., Sun, C., Castano, I., Flanders, N. C., Evans, A. M., Vitaku, E., McLeod, D. C., Lambeth, R. H., Chen, L. X., Gianneschi, N. C., Dichtel, W. R., *Angewandte Chemie International Edition* (2020) **59** (13), 5165 <https://doi.org/10.1002/anie.201913975>
80. Fan, Y., Zhang, J., Shen, Y., Zheng, B., Zhang, W., Huo, F., *Nano Research* (2021) **14** (1), 1 10.1007/s12274-020-3082-4
81. Hennessy, M. H., Soos, Z. G., Pascal, R. A., Girlando, A., *Chemical Physics* (1999) **245** (1), 199 [https://doi.org/10.1016/S0301-0104\(99\)00082-8](https://doi.org/10.1016/S0301-0104(99)00082-8)
82. So, F. F., and Forrest, S. R., *Physical Review Letters* (1991) **66** (20), 2649 10.1103/PhysRevLett.66.2649
83. Li, X., Sinks, L. E., Rybtchinski, B., Wasielewski, M. R., *Journal of the American Chemical Society* (2004) **126** (35), 10810 10.1021/ja047176b
84. Würthner, F., Thalacker, C., Sautter, A., Schärfl, W., Ibach, W., Hollricher, O., *Chemistry – A European Journal* (2000) **6** (21), 3871 [https://doi.org/10.1002/1521-3765\(20001103\)6:21<3871::AID-CHEM3871>3.0.CO;2-4](https://doi.org/10.1002/1521-3765(20001103)6:21<3871::AID-CHEM3871>3.0.CO;2-4)
85. Li, A. D. Q., Wang, W., Wang, L.-Q., *Chemistry – A European Journal* (2003) **9** (19), 4594 <https://doi.org/10.1002/chem.200305025>
86. Wang, W., Li, L.-S., Helms, G., Zhou, H.-H., Li, A. D. Q., *Journal of the American Chemical Society* (2003) **125** (5), 1120 10.1021/ja027186h
87. Langhals, H., and Ismael, R., *European Journal of Organic Chemistry* (1998) **1998** (9), 1915 [https://doi.org/10.1002/\(SICI\)1099-0690\(199809\)1998:9<1915::AID-EJOC1915>3.0.CO;2-1](https://doi.org/10.1002/(SICI)1099-0690(199809)1998:9<1915::AID-EJOC1915>3.0.CO;2-1)
88. van der Boom, T., Hayes, R. T., Zhao, Y., Bushard, P. J., Weiss, E. A., Wasielewski, M. R., *Journal of the American Chemical Society* (2002) **124** (32), 9582 10.1021/ja026286k
89. Würthner, F., *Chemical Communications* (2004) (14), 1564 10.1039/B401630K
90. Ghosh, S., Li, X.-Q., Stepanenko, V., Würthner, F., *Chemistry – A European Journal* (2008) **14** (36), 11343 <https://doi.org/10.1002/chem.200801454>
91. Yagai, S., Seki, T., Karatsu, T., Kitamura, A., Würthner, F., *Angewandte Chemie International Edition* (2008) **47** (18), 3367 <https://doi.org/10.1002/anie.200705385>

92. Kumar, M., and George, S. J., *Nanoscale* (2011) **3** (5), 2130 10.1039/C1NR10151J
93. Bell, T. D. M., Bhosale, S. V., Forsyth, C. M., Hayne, D., Ghiggino, K. P., Hutchison, J. A., Jani, C. H., Langford, S. J., Lee, M. A. P., Woodward, C. P., *Chemical Communications* (2010) **46** (27), 4881 10.1039/C0CC00865F
94. Basak, S., Nanda, J., Banerjee, A., *Chemical Communications* (2013) **49** (61), 6891 10.1039/C3CC43538E
95. Asir, S., Demir, A. S., Icil, H., *Dyes and Pigments* (2010) **84** (1), 1
<https://doi.org/10.1016/j.dyepig.2009.04.014>
96. Ledwon, P., Ovsianikova, D., Jarosz, T., Gogoc, S., Nitschke, P., Domagala, W., *Electrochimica Acta* (2019) **307**, 525 <https://doi.org/10.1016/j.electacta.2019.03.169>
97. Man, I. C., Su, H.-Y., Calle-Vallejo, F., Hansen, H. A., Martínez, J. I., Inoglu, N. G., Kitchin, J., Jaramillo, T. F., Nørskov, J. K., Rossmeisl, J., *ChemCatChem* (2011) **3** (7), 1159
<https://doi.org/10.1002/cctc.201000397>

Supporting information

Covalent organic frameworks based on electroactive naphthalenediimide active electrocatalysts toward oxygen reduction reaction

Marcos Martínez-Fernández,^{‡a} Emiliano Martínez-Periñán,^{‡b} Sergio Royuela,^c José I.

*Martínez,^d F. Zamora,^{cefg} Encarnación Lorenzo^{*bfg} and José L. Segura^{*a}*

^a Departamento de Química Orgánica I, Facultad de CC. Químicas, Universidad

Complutense de Madrid, 28040 Madrid, Spain. E-mail: segura@ucm.es

^b Departamento de Química Analítica y Análisis Instrumental, Facultad de Ciencias,

Universidad Autónoma de Madrid, 28049 Madrid, Spain.

E-mail: encarnacion.lorenzo@uam.es

^c Departamento de Nanoestructuras, Superficies, Recubrimientos y Astrofísica

Molecular, Instituto de Ciencia de Materiales de Madrid (ICMM-CSIC),

28049 Madrid, Spain

d Departamento de Química Inorgánica, Facultad de Ciencias, Universidad

Autónoma de Madrid, 28049 Madrid, Spain.

e Instituto Madrileño de Estudios Avanzados en Nanociencia (IMDEA-Nanociencia),

Cantoblanco, 28049 Madrid, Spain

f Institute for Advanced Research in Chemical Sciences (IAdChem), Universidad

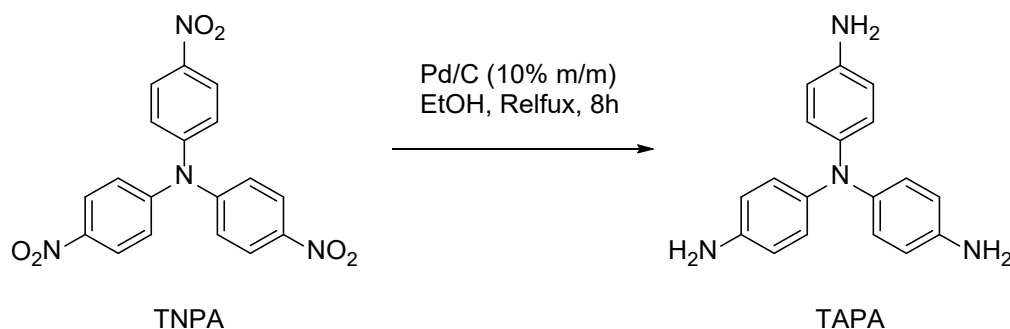
Autónoma de Madrid, 28049 Madrid, Spain

g Condensed MatterPhysics Center (IFIMAC), Universidad Autónoma de Madrid,

28049 Madrid, Spain

‡ These authors contributed equally to this work.

Synthesis of N-N'-N''-Tris-(4-aminofenil) amine **TAPA**.



TAPA synthesis was accomplished by following reported literature with slight modifications.[1] In a typical synthesis, under argon atmosphere **TNPA** (1g, 2.63 mmol) and Pd/C (10% wt, 150mg) are suspended in ethanol (32 mL). The mixture is heated to reflux to obtain a green solution. Then, 50-60% v/v hydrazine hydrate (1.03 mL, 16.57 mmol) was added dropwise during 3 h. The mixture was heated under reflux 8 hours. Once the reaction time was passed, hot-filtering over 1 cm Celite pad afforded pure **TAPA** by crystallization as a white solid. Vacuum filtration and subsequent recrystallizations yielded 631 mg (83%) of the triamine compound.

¹H NMR (300MHz, DMSO-d₆) δ(ppm): 6.59 (d, J = 8.7 Hz, 6H, Ph), 6.43 (d, J = 8.7 Hz, 6H, Ph), 4.69 (s, 6H, -NH₂).

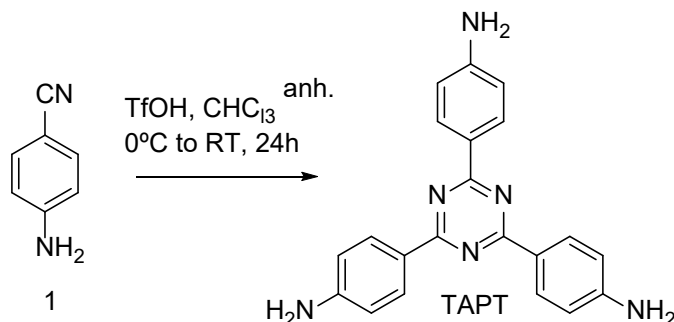
¹³C-NMR (75MHz, DMSO-d₆) δ(ppm): 143.66, 139.10, 124.53, 115.18.

FTIR (ATR) $\tilde{\nu}$ (cm⁻¹): 3402.7, 3330, 3025, 2295, 1605, 1498, 1324, 1253, 1166, 117, 822.

MS (ESI): Found C₁₈H₁₈N₄ [M]⁺ 290.9 m/z; Calcd C₁₈H₁₈N₄ [M]⁺ 290.15 m/z.

Melting point: 244-245 °C

Synthesis of 2,4,6-Tris (4-aminofenil)-1,3,5-triazine **TAPT**.



TAPT was synthesized according to toBhaumik et al. with a slight modification.[2] First, a (5 mL) anhydrous CHCl₃/ (1,7 ml) trifluoromethanesulfonic acid (TfOH) was prepared and degassed with argon. Separately, under argon atmosphere, a solution of 4-aminobenzonitrile **1** (500 mg, 4,23 mmol) is dissolved in 20 mL of anhydrous CHCl₃, degassed and added at 0°C to the CHCl₃/TfOH mixture, dropwise under intense stirring. Once the addition is finished the yellow mixture was warmed to room temperature and stirred 24 hours. Finally, neutralization with NaOH 2M precipitates **TAPT** compound, which is washed with water and methanol droplets to obtain 284 mg (57%) of the pure triamine compound as a pale yellow solid.

¹H NMR (300MHz, DMSO-d₆) δ(ppm): 8.36 (d, J = 8.0 Hz, 6H, Ph), 6.70 (d, J = 8.0 Hz, 6H, Ph), 5.90 (s, 6H, -NH₂).

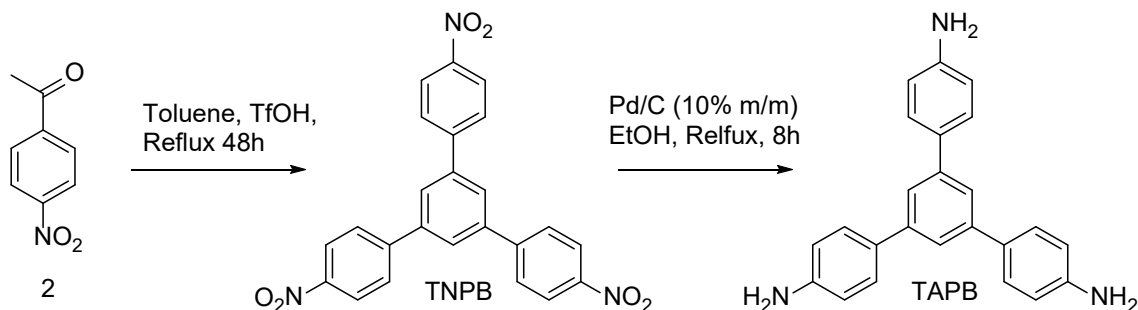
¹³C-NMR (75MHz, DMSO-d₆) δ(ppm):170.05, 153.45, 130.63, 123.40, 113.59.

FTIR (ATR) $\tilde{\nu}$ (cm⁻¹): 3459.7, 3374.8, 3319.9, 3207.5, 3027.5, 1633.9, 1602.0, 1577.5, 1493.0, 1425.8, 1362.4, 1291.9, 1178.8, 1147.3, 1126.1, 808.6, 586.5.

MS (ESI): Found C₂₁H₁₈N₆ [M]⁺355.0 m/z; Calcd C₂₁H₁₈N₆ [M]⁺354.16 m/z.

Melting point > 300 °C.

Synthesis of 1,3,5-Tris-(4-aminofenil) benzene **TAPB**.



TAPB was synthesized according to previously reported literature.[3] First, **TNPB** is obtained by cyclotrimerization reaction of 4-nitroacetophenone **2** (23g, 140mmol) in refluxing toluene, catalysed by TfOH (0,5 mL) in a round bottom flask equipped with a Dean-Stark apparatus for 48h. After cooling to room temperature, the slurry was filtered giving a black solid which is washed with boiling DMF till the solid turns grey. This product is insoluble in any common deuterated solvent.

FTIR (ATR) $\tilde{\nu}$ (cm⁻¹): 1596.1, 1507.7, 1344.2, 1249.2, 1105.4, 863.1, 840.4, 814.3, 748.5, 689.7.

Melting point >300 °C.

TAPB is synthesized by hydrazine reduction of nitro groups of **TNPB**. In a typical synthesis, under argon atmosphere, **TNPB** (5 g, 11,3 mmol) and 10% wt Pd/C (0.87 g) are suspended in ethanol (200 mL). The suspension was heated to reflux to obtain a grey solution, then 50-60% v/v hydrazine hydrate (43 mL, 0.5 mol) was added dropwise through an addition funnel. The mixture was refluxed overnight, hot filtered over 1 cm Celite pad and cooled to room temperature and then cooled in a fridge. The resulting crystallite is filtered under vacuum and washed with cold ethanol to afford 3.3 g (83%) of **TAPB** as yellow solid.

¹H NMR (300MHz, DMSO-d₆) δ(ppm): 7.53 – 7.43 (m, 9H, Ph), 6.66 (d, J = 8.5 Hz, 6H, Ph), 5.21 (s, 6H, -NH₂).

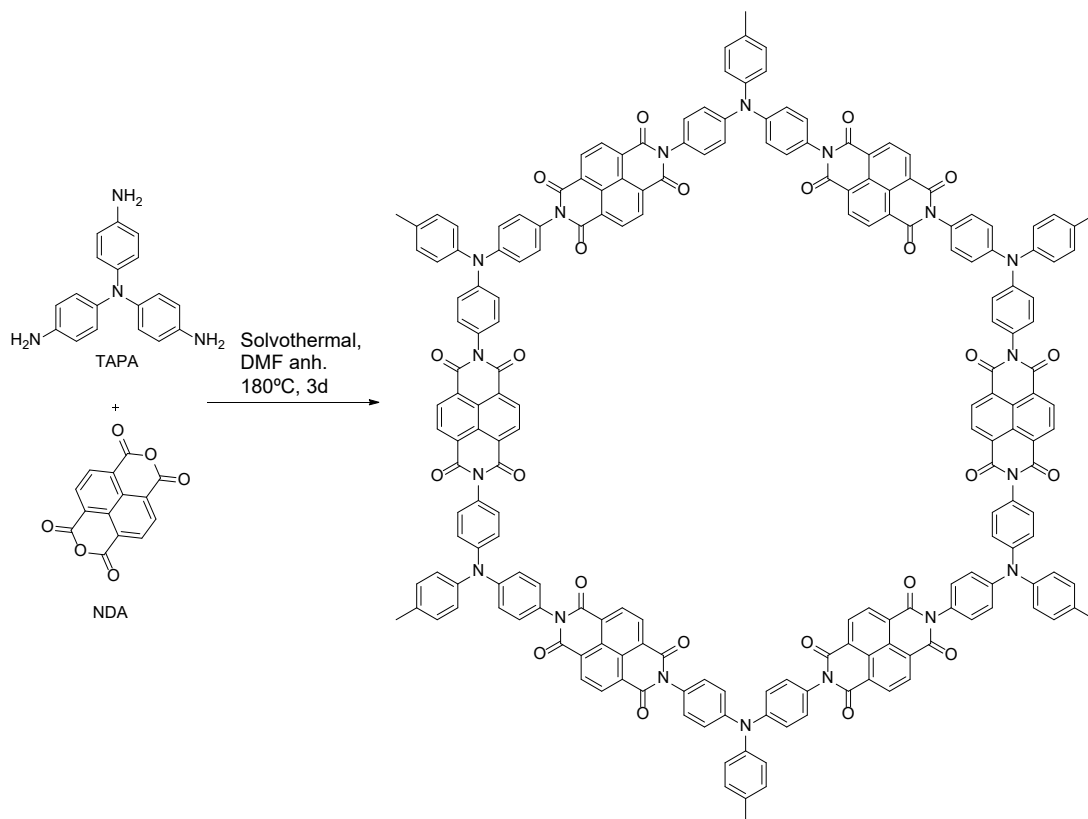
¹³C-NMR (75MHz, DMSO-d₆) δ(ppm):145.88, 141.99, 131.93, 128.23, 122.93, 115.39.

FTIR (ATR) $\tilde{\nu}$ (cm⁻¹):3434.4, 3343.6, 3221.6, 3029.2, 1612.6, 1511.1, 1450.9, 1404.2, 1280.1, 1177.9, 825.9, 559.7.

MS (ESI): Found C₂₁H₁₈N₆ [M]⁺352.1 m/z; Calcd C₂₁H₁₈N₆ [M]⁺351.17 m/z.

Melting point>261- 262 °C.

Synthesis of **TAPA-NDI-COF**.



In a Pyrex tube (14 mm internal diameter, 11 cm height), **TAPA** (29 mg, 0.1 mmol) and **NDA** (40.2 mg, 0.15 mmol) were suspended, under argon atmosphere, in anhydrous N,N'-Dimethylformamide (DMF). The mixture was sonicated for 5 minutes to obtain a homogenous dispersion. The tube was degassed via three freeze-pump-thaw cycles, flame sealed and heated at 180 °C for 3 days. The precipitate was collected by filtration and washed with hot DMF (120 °C) 6 times for a day, hot THF (50 °C) 6 times for a day, ethanol 3 times for half day and hexane 3 times for half day. Finally, 52.3 mg (83%) of **TAPA-NDI-COF** was obtained as a grey-purple solid. All the experimental data was in good agreement with the reported in literature.[4]

^{13}C -NMR (CP/MAS) $\delta(\text{ppm})$:163.19, 148.01, 128.59.

FTIR (ATR) $\tilde{\nu}$ (cm^{-1}): 1713.62, 1666.87, 1620.79, 1578.81, 1498.89, 1447.25, 1343.41, 1318.49, 1286.42, 1241.29, 1192.48, 1133.35, 1133.35, 979.9, 852.2, 827.3, 765.61, 749.1, 728.78, 709.9, 626.24.

PDRX (2θ $^\circ$): 3.35, 6.5, 8.62.

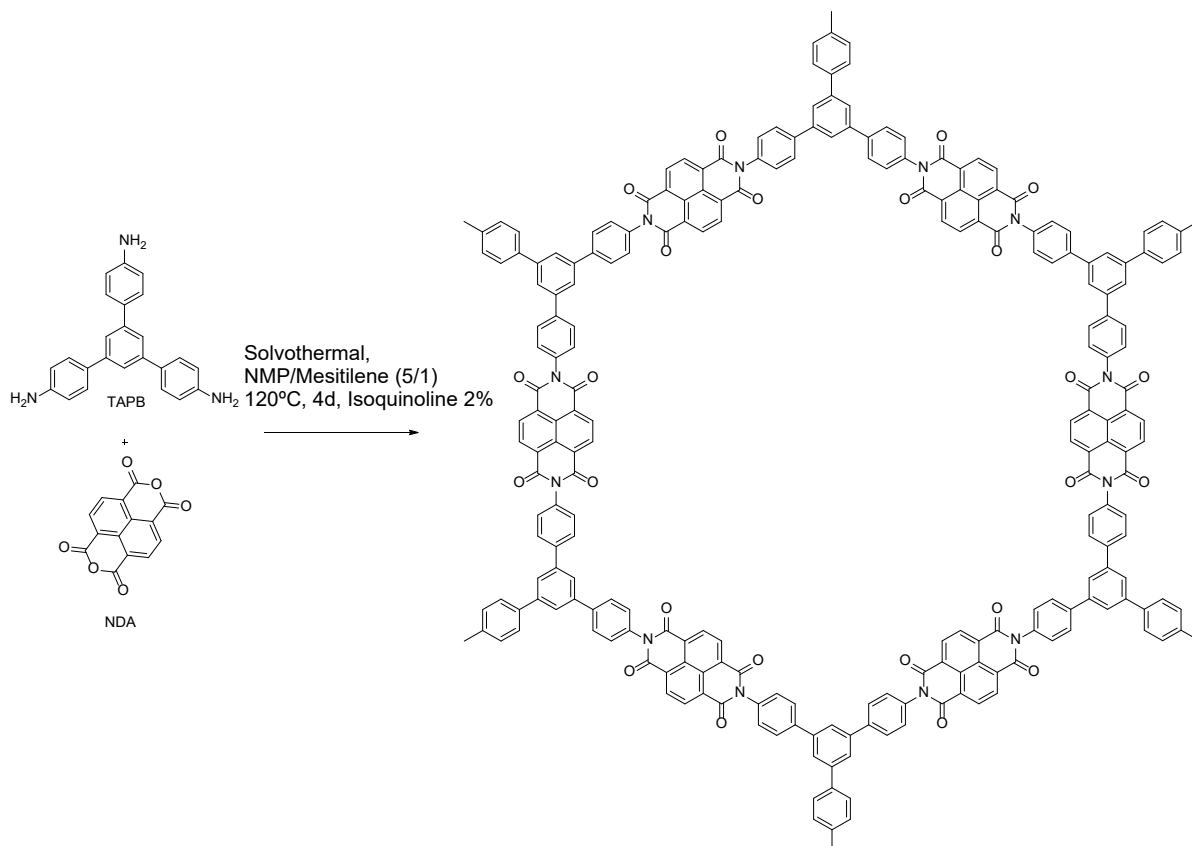
Porosity: Bet surface: $1283 \text{ m}^2\text{g}^{-1}$, pore volume at 0.95 p/p $^\circ$ $0.839 \text{ cm}^3\text{g}^{-1}$, pore size 2.3 nm.

TGA: Stable until 587 $^\circ\text{C}$.

Unit cell: $\text{C}_{78}\text{N}_8\text{O}_{12}\text{H}_{36}$

Microanalysis: Found for $\text{C}_{78}\text{N}_8\text{O}_{12}\text{H}_{36} \cdot 15\text{H}_2\text{O}$ %C:60,62 %N: 7,26; %H: 3,13; %O: 28,99.
Calculated: %C:60,9; %N:8,78; %H:3,3; %O:27,02.

Synthesis of **TAPB-NDI-COF**.



In a Pyrex tube (14 mm internal diameter, 11 cm height), **TAPB** (35,1 mg, 0.1 mmol), **NDA** (40.2 mg, 0.15 mmol) and isoquinoline (2% v/v, 0,015 mL) were suspended in a mixture of 0,75 mL N-methyl-2-pirrolidone (NMP) and 0,15 mL mesitylene. The mixture was sonicated for 5 minutes to obtain a homogenous dispersion. The tube was degassed via three freeze-pump-thaw cycles, flame sealed and heated at 120 °C for 4 days. The precipitate was collected by filtration and washed with hot DMF (120°C) 6 times for a day, hot THF (50°C) 6 times for a day, ethanol 3 times for half day and hexane 3 times for half day. Finally, 64.7 mg (94%) of **TAPB-NDI-COF** was obtained as a pale yellow solid. All the experimental data was in good agreement with the reported in literature.[5]

^{13}C -NMR (CP/MAS) $\delta(\text{ppm})$:163.75, 143.3, 129.5.

FTIR (ATR) $\tilde{\nu}$ (cm^{-1}): 1713.36, 1673.46, 1618.23, 1578.34, 1504.79, 11443.63, 1335.43, 1224.77, 1189.55, 1132.1, 1111.99, 1021.65, 981.76, 884.64, 862.38, 822.48, 789.6, 758.64, 707.56.

PDRX (2θ $^\circ$): 3.01, 5.71, 7.31.

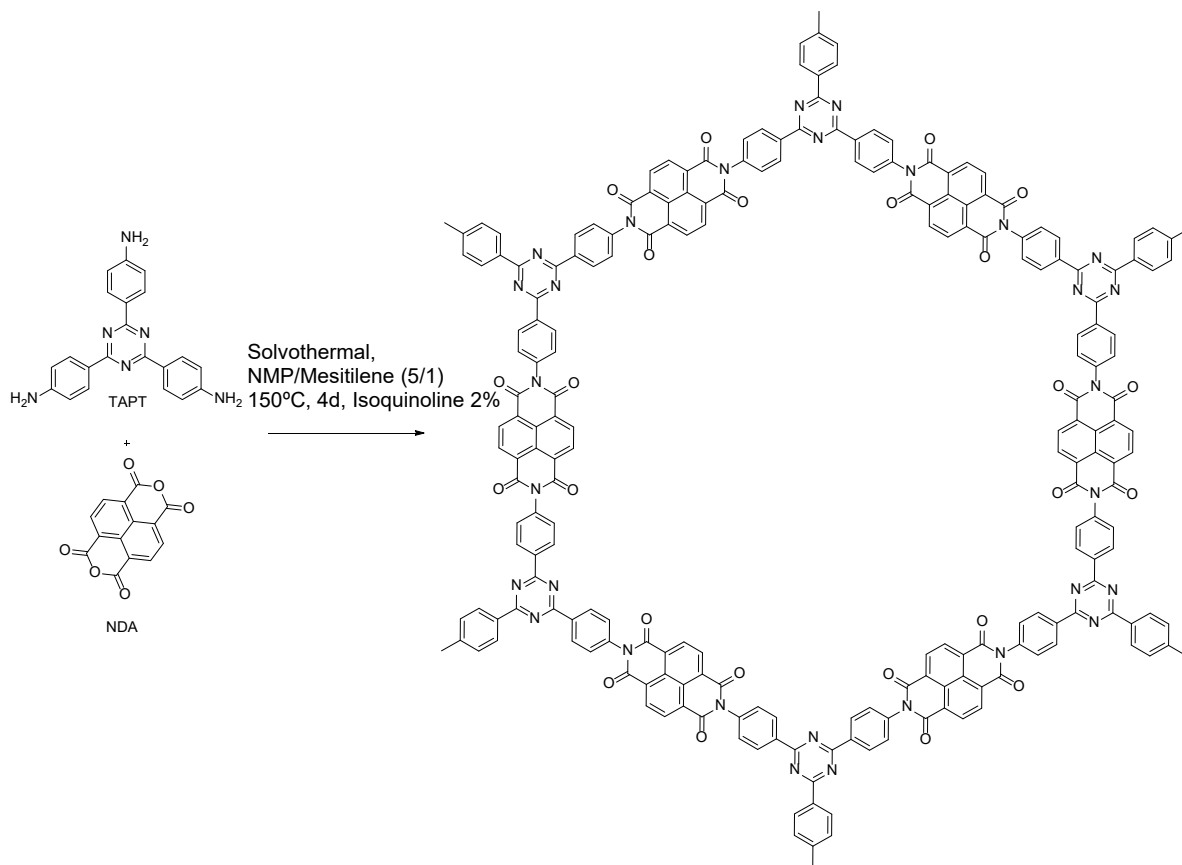
Porosity: Bet surface: $1138\text{m}^2\text{g}^{-1}$, pore volume at 0.95 p/p $^\circ$ $0.777\text{ cm}^3\text{g}^{-1}$, pore size 2.6 nm.

TGA: Stable until 594 $^\circ\text{C}$.

Unit cell: $\text{C}_{90}\text{N}_6\text{O}_{12}\text{H}_{42}$

Microanalysis: Found for $\text{C}_{90}\text{N}_6\text{O}_{12}\text{H}_{42} \cdot 8\text{H}_2\text{O}$ %C:70,03; %N: 5,45; %H: 3,78; %O:20,73.
Calculated: %C:70,25; %N:5,63; %H:4,03; %O:20,09.

Synthesis of TAPT-NDI-COF.



In a Pyrex tube (14 mm internal diameter, 11 cm height), **TAPT** (35,4 mg, 0.1 mmol), **NDA** (40.2 mg, 0.15 mmol) and isoquinoline (2% v/v, 0,015 mL) were suspended in a mixture of 0,75 mL N-methyl-2-pyrrolidone (NMP) and 0,15 mL mesitylene. The mixture was sonicated for 5 minutes to obtain a homogenous dispersion. The tube was degassed via three freeze-pump-thaw cycles, flame sealed and heated at 150 °C for 4 days. The precipitate was collected by filtration and washed with hot DMF (120°C) 6 times for a day, hot THF (50°C) 6 times for a day, ethanol 3 times for half day and hexane 3 times for half day. Finally, 52,3 mg (81%) of **TAPT-NDI-COF** was obtained as a tile red solid. Screening conditions are summarized in Table S1.

¹³C-NMR (CP/MAS) δ (ppm): 171.62, 163.75, 138.05, 130.16.

FTIR (ATR) $\tilde{\nu}$ (cm^{-1}): 1713.22, 1671.43, 1578.46, 1506.38, 1446.39, 1411.01, 1333.59, 1243.59, 1187.33, 817.43, 793.60, 766.2, 751.99, 721.22, 715.5, 666.92, 657.92, 636.03, 635.05, 626.

PDRX (2θ °): 3.01, 5.71, 7.31.

Porosity: Bet surface: $501 \text{ m}^2\text{g}^{-1}$, pore volume at 0.95 p/p° $0.596 \text{ cm}^3\text{g}^{-1}$, pore size 2.6 nm.

TGA: Stable until 594 °C.

Unit cell: $\text{C}_{84}\text{N}_{12}\text{O}_{12}\text{H}_{36}$

Microanalysis: Found for $\text{C}_{84}\text{N}_{12}\text{O}_{12}\text{H}_{36} \cdot 17\text{H}_2\text{O}$ %C: 58,94; %N: 9,82; %H: 4,12; %O: 27,10.
Calculated: %C: 58,89; %N: 10,01; %H: 3,32; %O: 27,69.

Table S1. Screening of conditions for the synthesis of **TAPT-NDI-COF** (NMP=N-methyl-2-pyrrolidone, Mes=mesitilene, oDCB=1,2-dichlorobenzene, DMF=N,N'-dimethylformamide, PFH=perfluorohexane, EtOH=ethanol, H=hexane).

Solvent mixture	Isoquinoline (%)	Concentration NDA+TAPT (mg/mL)	T (°C)	Time (days)	Whases	Crystallinity
NMP:Mes (5:1)	2,00	82,8	120	4	DMF(RT), EtOH(RT), THF(RT)	Low
NMP:Mes (1:1)	2,00	82,8	120	4	DMF(RT), EtOH(RT), THF(RT)	No
NMP:Mes (1:5)	2,00	82,8	120	4	DMF(RT), EtOH(RT), THF(RT)	No
NMP:Mes (1:1)	2,00	82,8	180	4	DMF(RT), EtOH(RT), THF(RT)	Verylow
NMP:Mes (5:1)	2,00	82,8	180	4	DMF(RT), EtOH(RT), THF(RT)	Verylow
NMP:Mes (1:1)	2,00	82,8	150	4	DMF(RT), EtOH(RT), THF(RT)	Verylow
NMP:Mes (1:2)	2,00	82,8	150	4	DMF(RT), EtOH(RT), THF(RT)	No
NMP:Mes (2:1)	2,00	82,8	150	4	DMF(RT), EtOH(RT), THF(RT)	Verylow
NMP:Mes (5:1)	2,00	82,8	150	4	DMF(RT), EtOH(RT), THF(RT)	Moderate
NMP:Mes (5:1)	2,00	41,4	150	4	DMF(RT), EtOH(RT), THF(RT)	Low
NMP	2,00	82,8	150	4	DMF(RT), EtOH(RT), THF(RT)	Low
NMP:DMF(5:1)	2,00	82,8	150	4	DMF(RT), EtOH(RT), THF(RT)	Low
NMP:Mes (8:1)	2,00	82,8	150	4	DMF(RT), EtOH(RT), THF(RT)	Low
NMP:oDCB(5:1)	2,00	82,8	150	4	DMF(RT), EtOH(RT), THF(RT)	Low
NMP:Mes (5:1)	1,00	82,8	150	4	DMF(RT), EtOH(RT), THF(RT)	Low
NMP:Mes (5:1)	2,00	82,8	150	4	DMF (80°C), THF (RT), PFH (RT)	No
NMP:Mes (5:1)	2,00	82,8	150	4	DMF(RT), THF(RT),H (RT)	Moderate

NMP:Mes (5:1)	2,00	82,8	150	4	DMF(80°C), THF(RT),H (RT)	Moderate
NMP:Mes (5:1)	2,00	82,8	150	4	DMF(120°C), THF(50°C), H (RT)	High
NMP:Mes (5:1)	2,00	82,8	150	5	DMF(RT), EtOH(RT), THF(RT)	Low

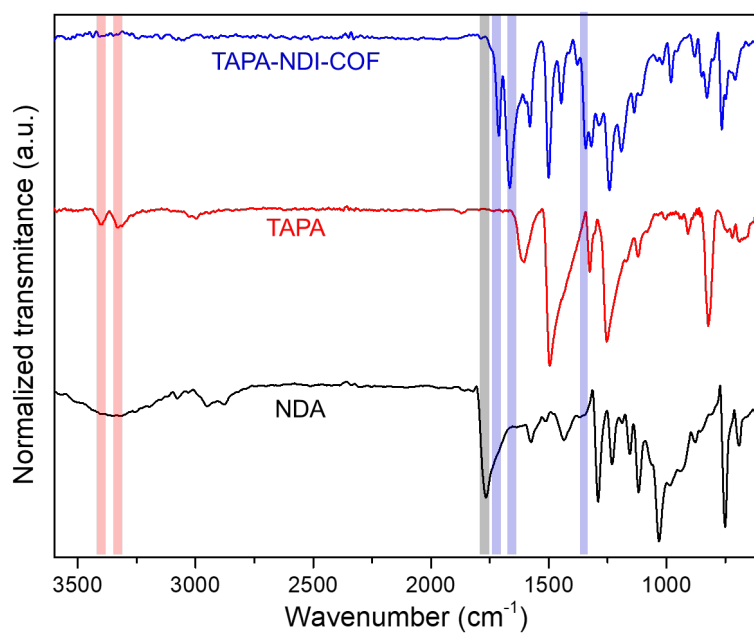


Figure. S1. FTIR analysis of **TAPA-NDI-COF**

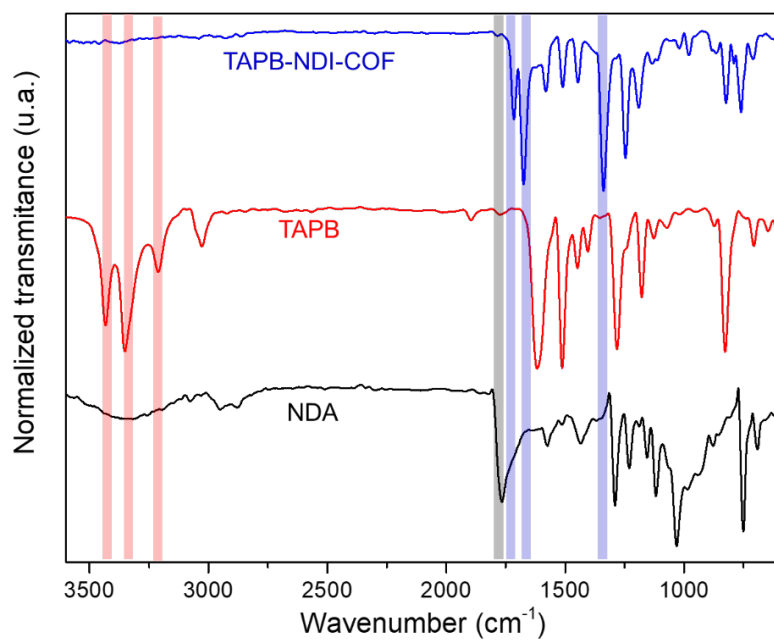


Figure. S2. FTIR analysis of **TAPB-NDI-COF**.

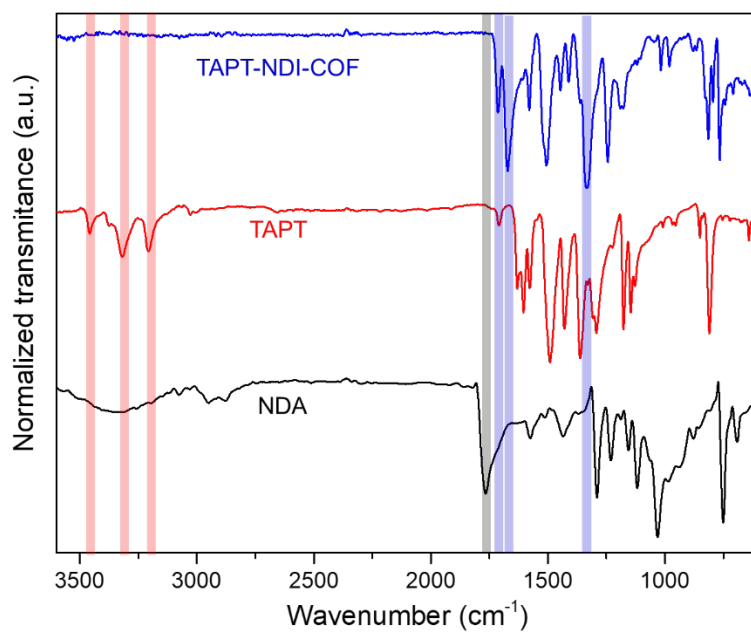


Figure. S3. FTIR analysis of **TAPT-NDI-COF**.

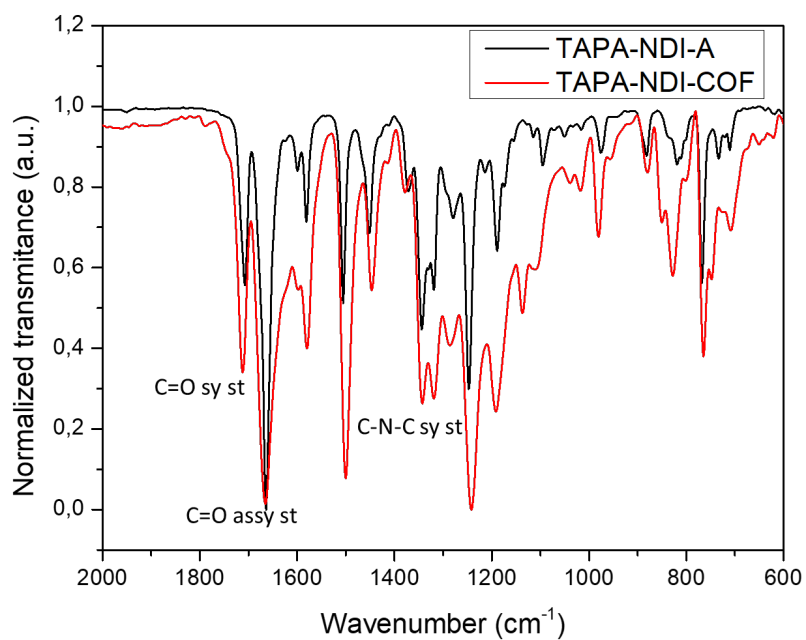


Figure. S4. FTIR comparison between **TAPA-NDI-COF** and **TAPA-NDI-A**.

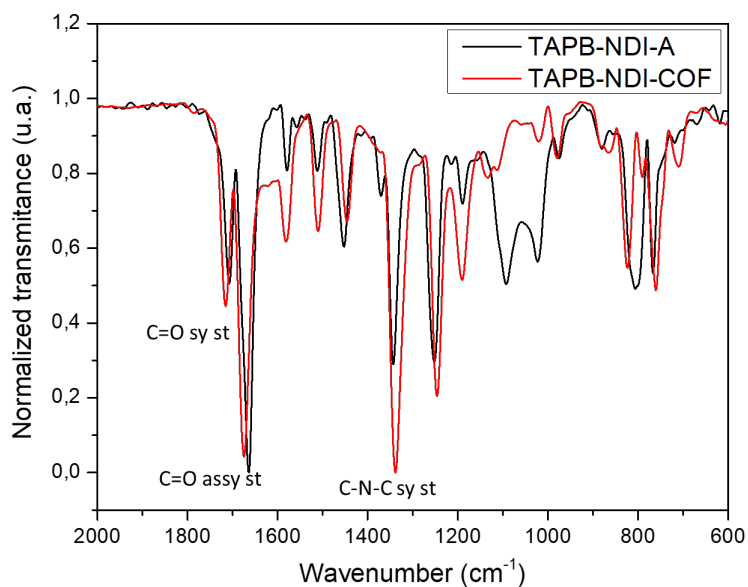


Figure. S5. FTIR comparison between **TAPB-NDI-COF** and **TAPB-NDI-A**.

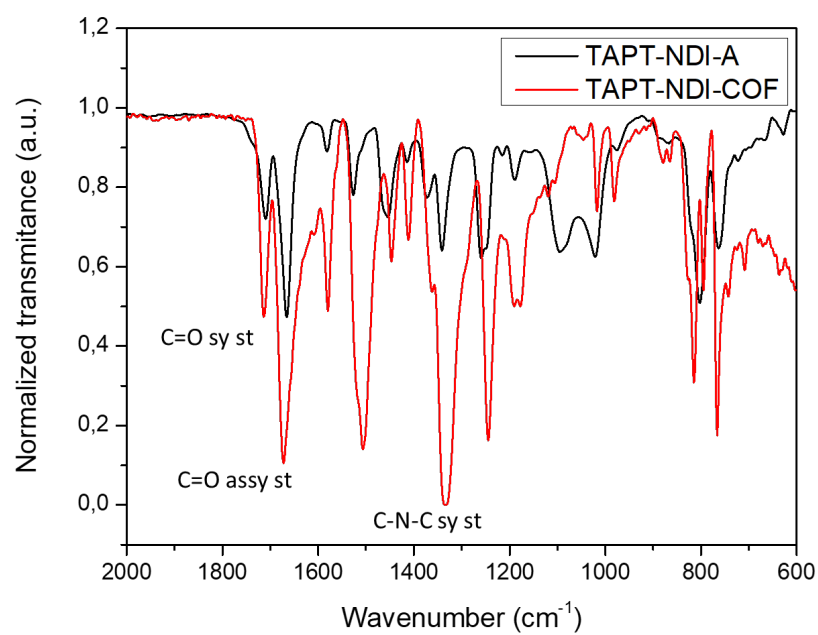


Figure. S6. FTIR comparison between **TAPT-NDI-COF** and **TAPT-NDI-A**.

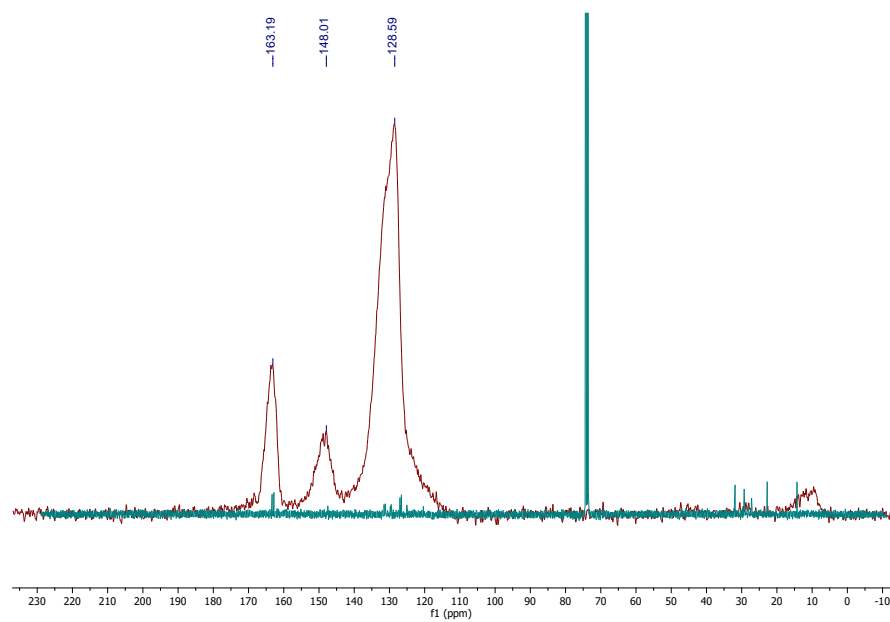


Figure. S7. ^{13}C -NMR comparison between **TAPA-NDI-COF** and **TAPA-NDI-A**.

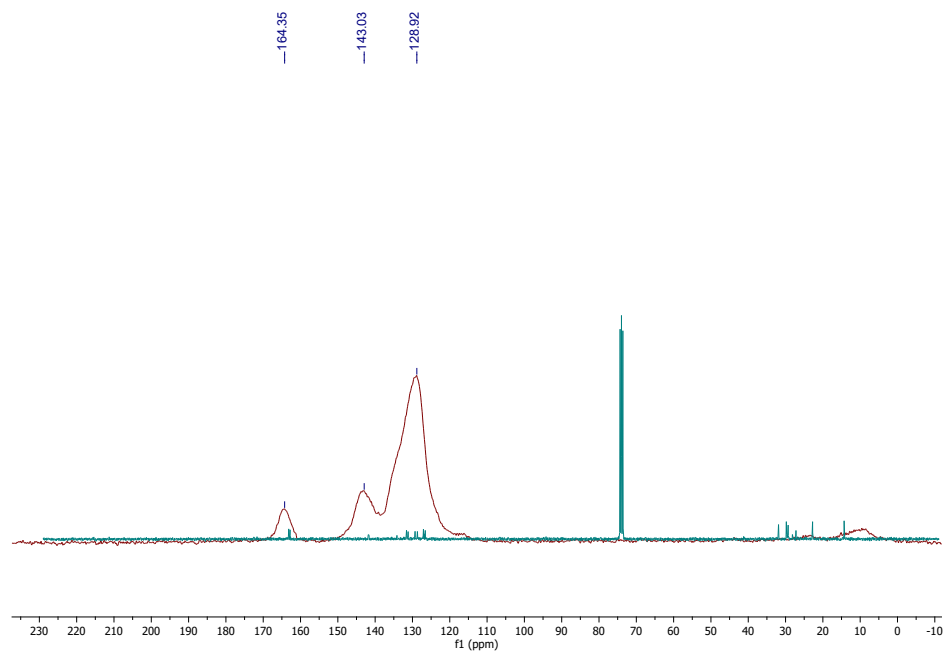


Figure. S8. ^{13}C -NMR comparison between TAPB-NDI-COF and TAPB-NDI-A.

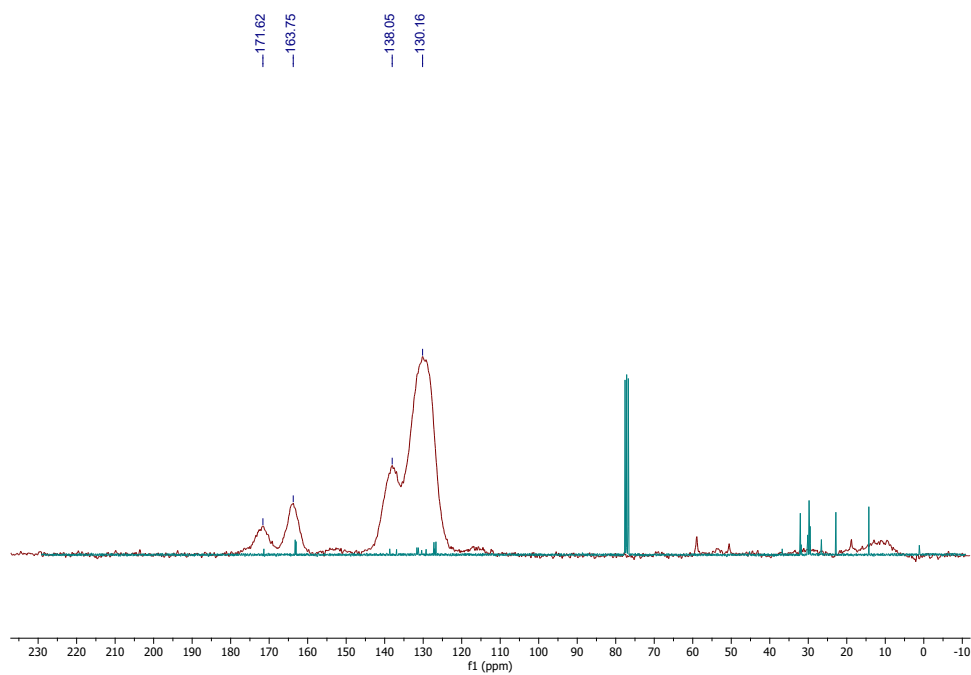


Figure. S9. ^{13}C -NMR comparison between TAPT-NDI-COF and TAPT-NDI-A.

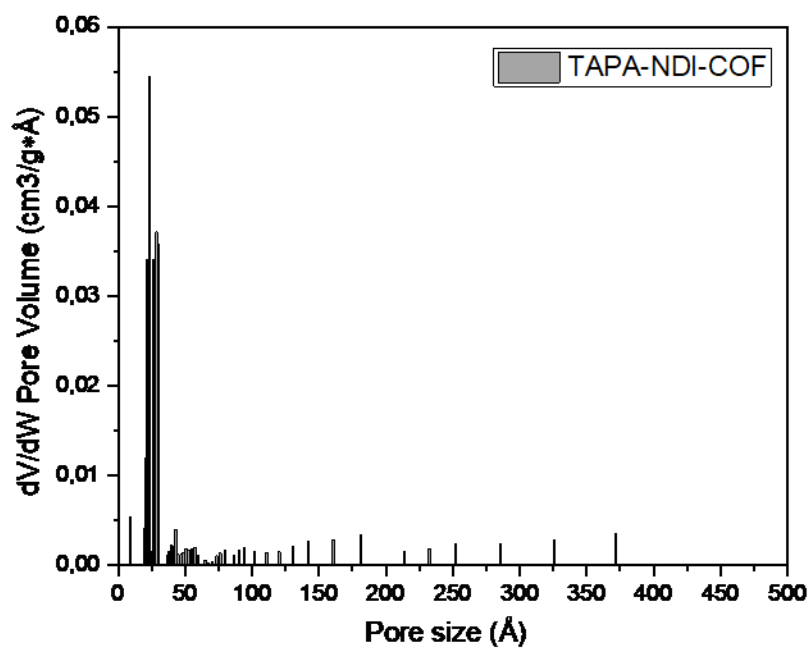


Figure. S10. Pore size distribution of TAPA-NDI-COF.

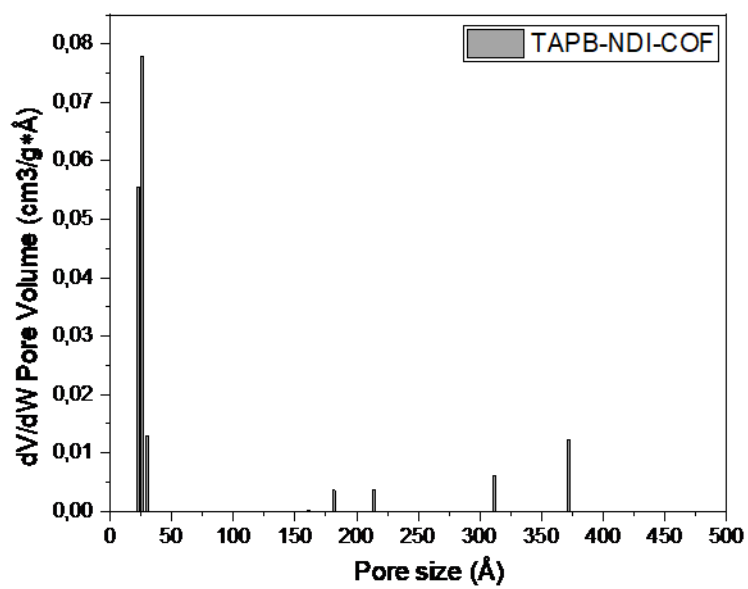


Figure. S11. Pore size distribution of TAPB-NDI-COF.

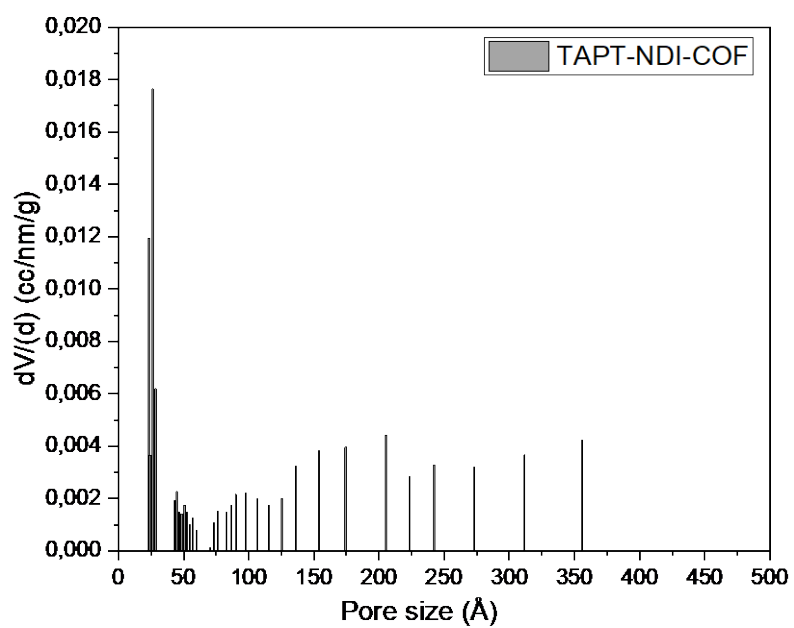


Figure. S12. Pore size distribution of TAPT-NDI-COF.

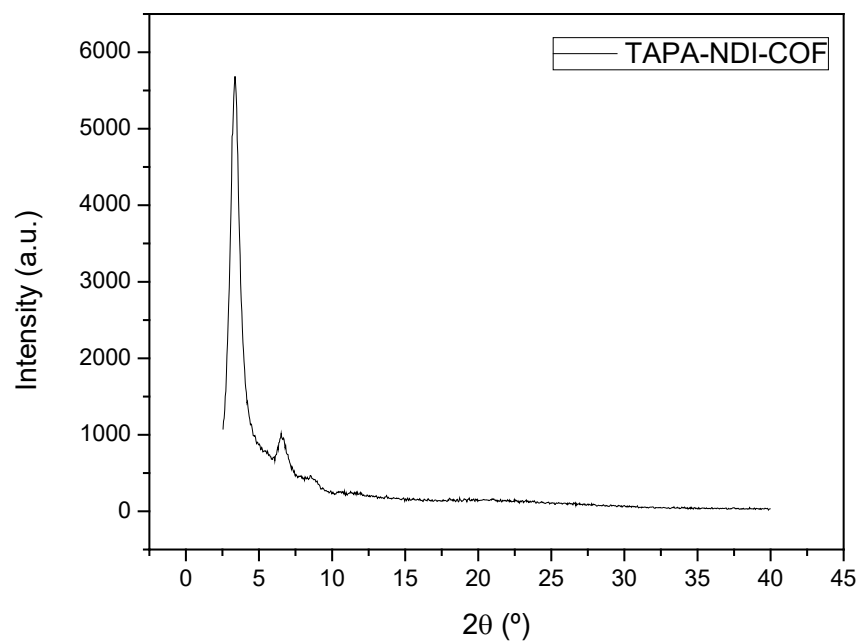


Figure. S13. Powder X-Ray diffractogram of TAPA-NDI-COF.

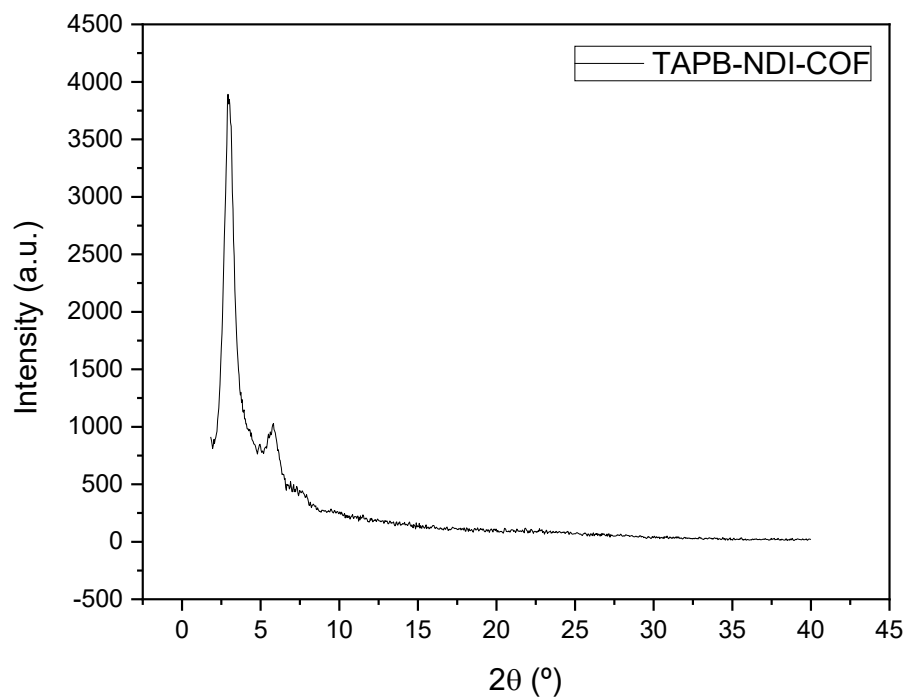


Figure. S14. Powder X-Ray diffractogram of TAPB-NDI-COF.

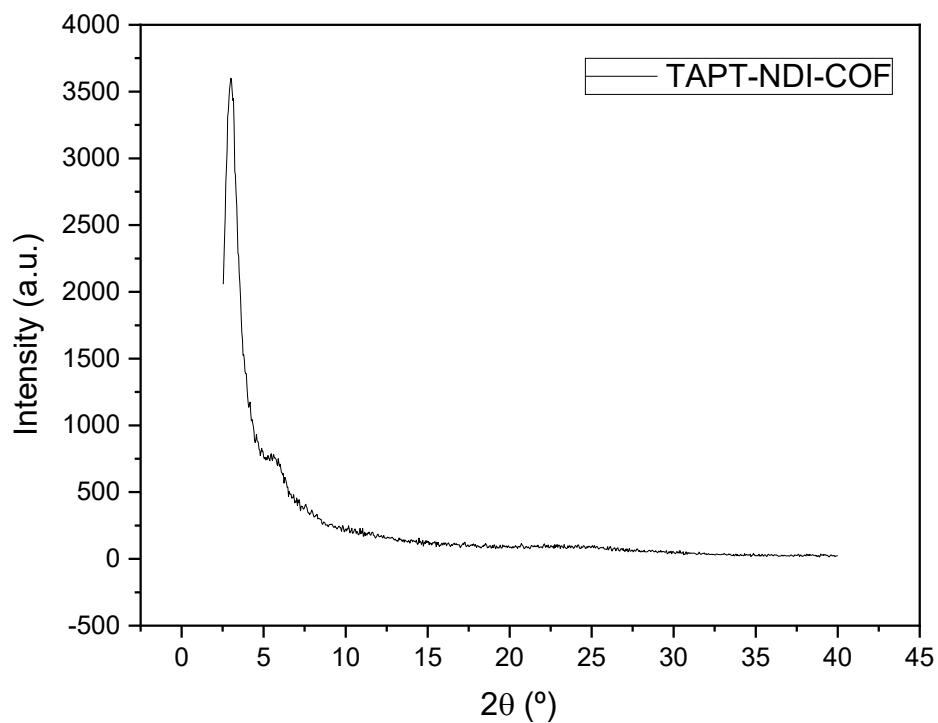


Figure. S15. Powder X-Ray diffractogram of TAPT-NDI-COF.

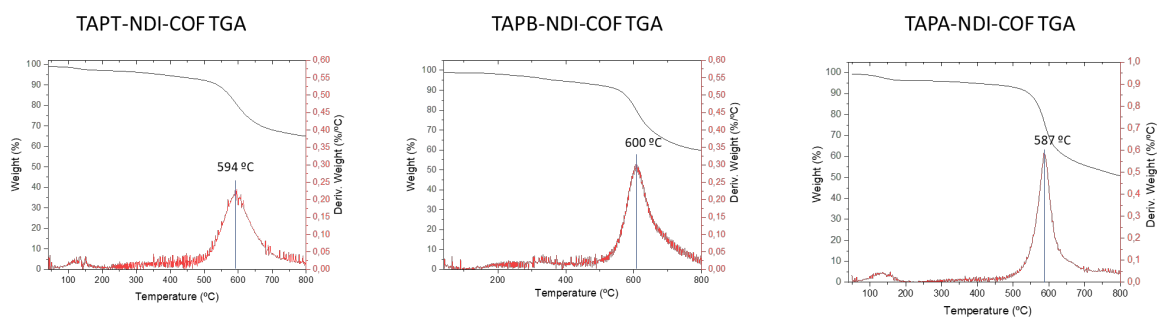


Figure. S16. Thermogravimetric analysis of TAPX-NDI-COFs.

Exfoliation procedure of COFs

TAPX-NDI-COF (1 mg) and 5 mL of EtOH/water (7/3) mixture were added to a 20 mL vial. Liquid phase exfoliation was performed in anT460/H ultrasonic bath for 5 minutes and the resulting suspension was centrifuged at 5000 rpm for 5 min to eliminate non-exfoliated COF. Finally, the supernatant was collected and transferred to a vial

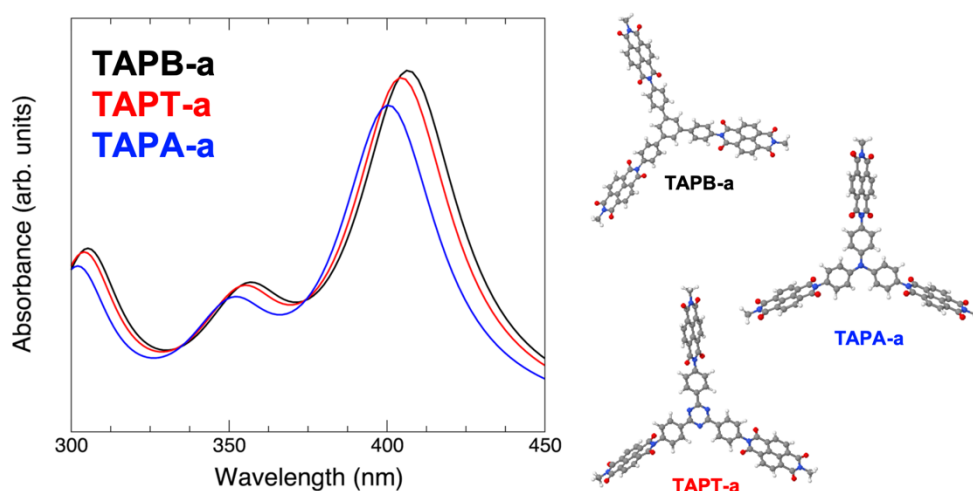


Figure S17. Photoabsorption spectra of the representative TAPB-NDI, TAPT-NDI and TAPA-NDI molecular units. The continuous curves are obtained by broadening the individual lines with gaussian curves of 0.2 eV width.

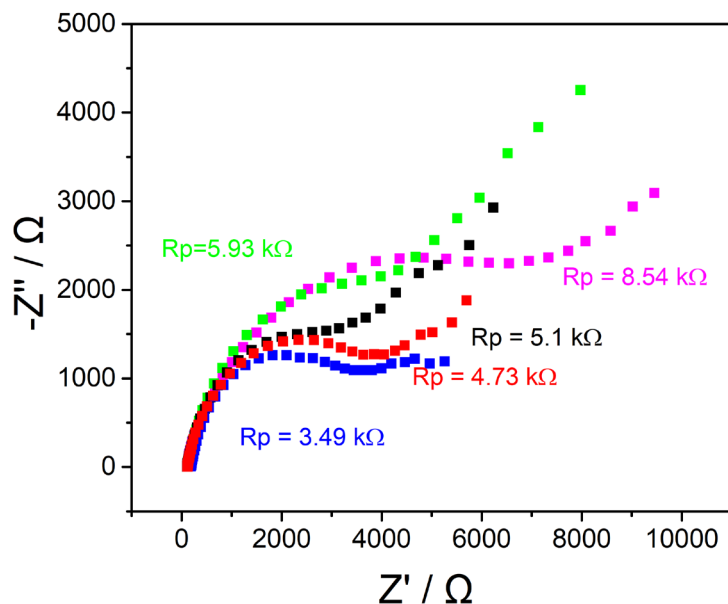


Figure S18. Nyquist plots (applied voltage $E = -0.4$ V vs. SCE, using an amplitude of 0.05 V and frequencies range from 0.1 to 80000 Hz) for bare GC disc electrode (pink), and GC electrodes modified with carbon SuperP (green), TAPA-NDI-COF-SuperP (blue), TAPT-NDI-COF-SuperP (black), and TAPB-NDI-COF-SuperP (red) in a O_2 saturated 0.1 M NaOH solution.

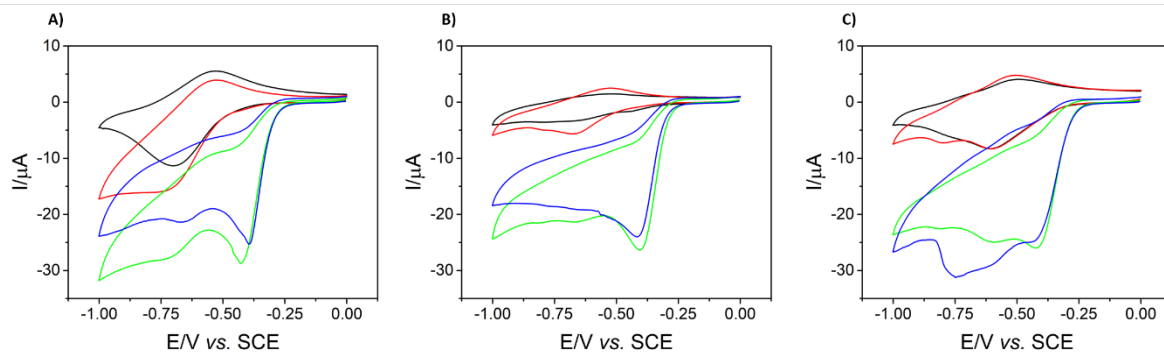
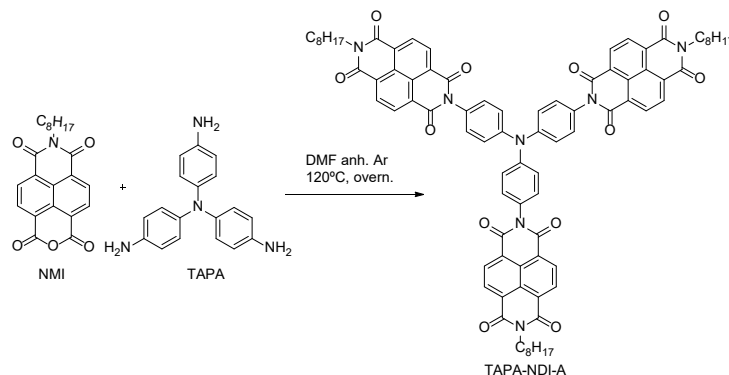


Figure S19. Cyclic voltammograms of GC electrodes modified with TAPB-NDI-COF-SuperP A), TAPT-NDI-COF-SuperP B), and TAPA-NDI-COF-SuperP C) in N_2 saturated 0.1 M NaOH solution in the absence of H_2O_2 (black) and in the presence of 1 mM H_2O_2 (red) or in O_2 saturated 0.1 M NaOH solution in the absence (blue) and in the presence of 1 mM H_2O_2 (green).

Table S2. Different metal free and non-pyrolized COF ORR electrocatalysts.

Compound	Onset potential	Preferent pathway	Additives	Reference
Covalent triazine framework (CTF)	0.0 V vs. SCE	4e ⁻	Nafion	Catal. Commun. 2015, 66, 91
Covalent organic radical framework (CORF)	-0.21 V vs. SCE	4e ⁻	Carbon Black	Angew. Chem. Int. Ed. 2018, 57,8007
Thiophene-Sulfur Covalent Organic Frameworks	-0.31 V vs. SCE	4e ⁻	Acetylene black and Nafion	J. Am. Chem. Soc. 2020, 142, 18, 8104
TAPA-NDI-COF	-0.31 V vs. SCE	4e ⁻	Carbon SuperP and Nafion	This Work
TAPB-NDI-COF	-0.32 V vs. SCE	4e ⁻	Carbon SuperP and Nafion	This Work
TAPT-NDI-COF	-0.32 V vs. SCE	4e ⁻	Carbon SuperP and Nafion	This Work
Co-N ₄ (O)	-0.209 V vs. SCE	2e ⁻	Nafion	Nat. Mater. 2020, 19, 436
Mo-S ₄	-0.229 V vs. SCE	2e ⁻	Acetylene black and Nafion	Angew. Chem. 2020, 59, 9171
FeN ₄ S ₂	-0.009V vs. SCE	4e ⁻	Nafion	J. Am. Chem. Soc. 2019, 141, 20118
CoNi-Sas/NC	-0.129V vs. SCE	4e ⁻	Nafion	Adv. Mater. 2019, 31, 1905622

Synthesis of **TAPA-NDI-A**.



In a two-neck round bottom flask, **NMI** (104.83 mg, 0.28 mmol) and **TAPA** (12.26 mg, 0.056 mmol) were added under argon atmosphere and dissolved in anhydrous DMF. The reaction was heated at 120°C overnight. The next day water was added to precipitate the product, which was vacuum-filtered and washed with water and methanol droplets. Finally, column chromatography (silica gel, DCM/MeOH 100/1) yield 27,9 mg (35%) **TAPA-NDI-A** as a grey-purple solid.

^1H NMR (300MHz, CHCl_3) δ (ppm): 8.8 (m, 12H), 7.46 (d, $J = 8.8$ Hz, 6H), 7.28 (d, $J = 8.8$ Hz, 6H), 4.22 (m, 6H), 1.75-1.34 (m, 36H), 0.87 (m, 9H).

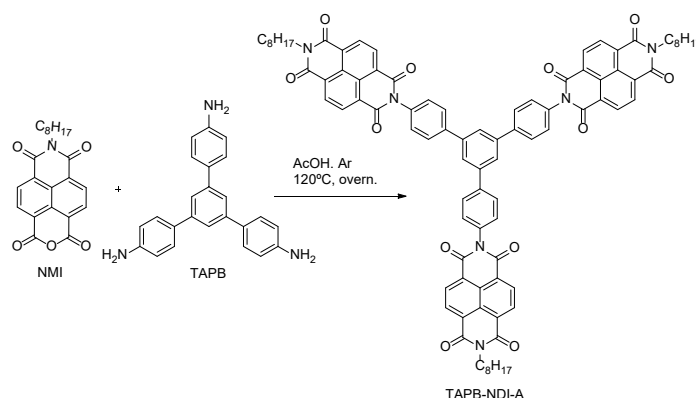
^{13}C -NMR (75MHz, TCE-d_2) δ (ppm): 163.16, 162.64, 147.37, 131.38, 131.02, 129.60, 129.37, 126.82, 126.66, 126.42, 124.93, 120.24, 31.74, 29.25, 29.21, 27.83, 27.06, 22.62, 14.17.

FTIR (ATR) $\tilde{\nu}$ (cm^{-1}): 2910.8, 1709.0, 1664.1, 1586.5, 1505.2, 1452.8, 1369.9, 1345.1, 1326.8, 1317.6, 1280.7, 1246.3, 1189.5, 959.3, 767.1.

MS (MALDI): Found $\text{C}_{84}\text{H}_{75}\text{N}_7\text{O}_{12}$ $[\text{M}]^+$ 1373.572 m/z; Calcd $\text{C}_{84}\text{H}_{75}\text{N}_7\text{O}_{12}$ $[\text{M}]^+$ 1373.55 m/z.

Melting point $>300^\circ\text{C}$.

Synthesis of **TAPB-NDI-A**.



In a two-neck round bottom flask, **NMI** (104.83 mg, 0.28 mmol) and **TAPB** (20 mg, 0.056 mmol) were added under argon atmosphere and dissolved in hot glacial acetic acid. The reaction was heated at 120 °C overnight. The next day a yellow precipitate was hot vacuum-filtered and washed with water and methanol droplets. Finally, column chromatography (silica gel, DCM/MeOH 100/1) yield 42,5 mg (52%) **TAPB-NDI-A** as an orange solid.

¹H NMR (300MHz, CHCl₃) δ(ppm): 8.74 (s, 12H, NDI), 8.09 – 7.77 (m, 9H), 7.45 (d, J = 6.3 Hz, 6H), 4.30 – 3.91 (m, 6H), 1.27 – 1.14 (m, 36H), 0.80 (s, 9H).

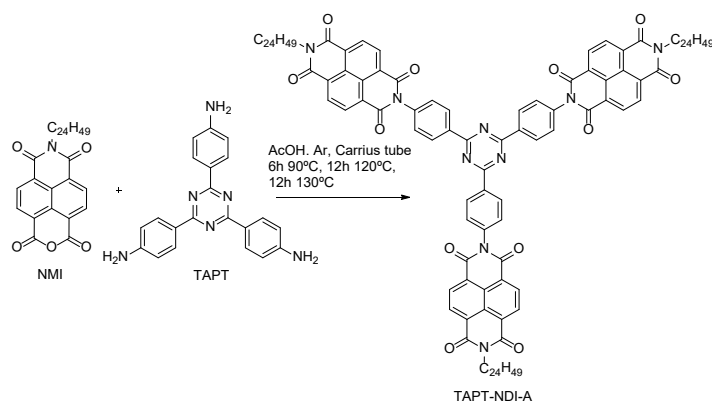
¹³C-NMR (75MHz, TCE-d₂) δ(ppm): 163.13, 162.73, 141.86, 141.56, 134.07, 131.51, 131.05, 129.13, 128.56, 127.15, 127.00, 126.96, 126.83, 126.54, 31.98, 31.87, 29.80, 29.46, 29.44, 29.31, 22.62, 14.23.

FTIR (ATR) $\tilde{\nu}$ (cm⁻¹): 2962.18, 2921.82, 2856.12, 1709.26, 1666.07, 1453.24, 1374.14, 1341.57, 1254.19, 1187.52, 1093.18, 1027.41, 807.06.

MS (MALDI): Found C₉₀H₇₈N₆O₁ [M+H]⁺ 1435.633 m/z; Calcd C₉₀H₇₈N₆O₁ [M]⁺ 1434.57 m/z.

Melting point >300 °C.

Synthesis of **TAPT-NDI-A**.



In a Carrius tube, **NMI** (136.83 mg, 0.22 mmol) and **TAPT** (20 mg, 0.056 mmol) were added under argon atmosphere and dissolved in glacial acetic acid (7 mL). The reaction was heated at 90 °C for 6 hours, at 120°C for 12 hours and at 130°C for 12 hours. A yellow precipitate was hot vacuum-filtered and washed with water and methanol droplets. Finally, column chromatography (silica gel, DCM/MeOH 100/1) yield 36mg (35%) **TAPT-NDI-A** as a yellow solid.

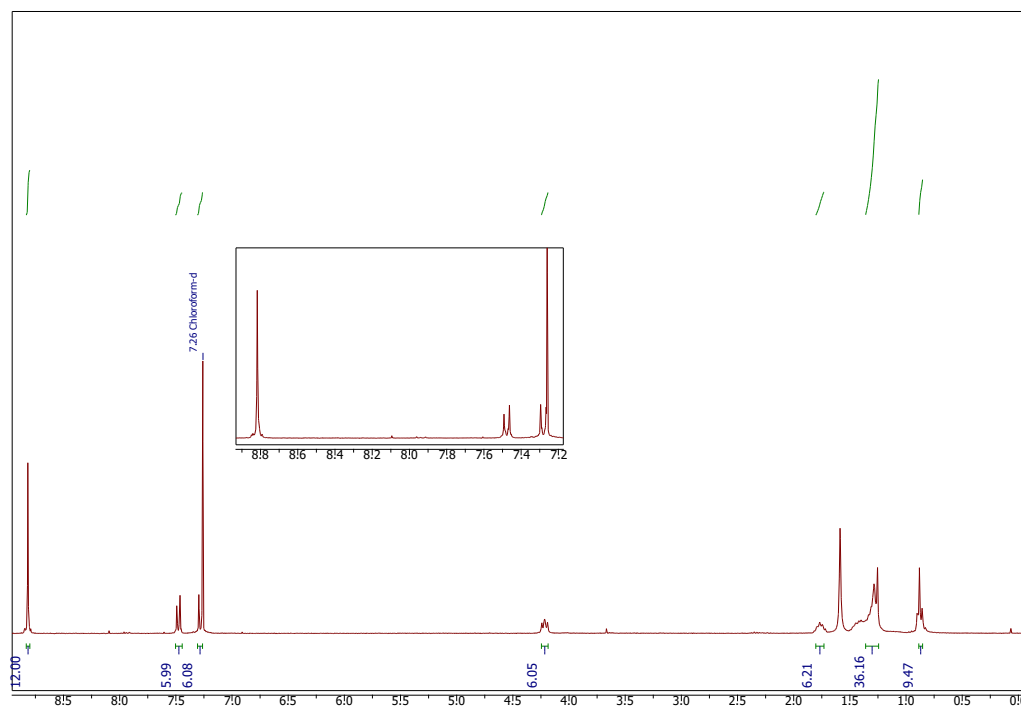
¹H NMR (300MHz, CHCl₃) δ(ppm): 9.03 (d, J = 8.6 Hz, 6H), 8.84 (m, 12H), 7.58 (d, J = 8.7 Hz, 6H), 4.17 (d, J = 7.0 Hz, 3H), 1.28 – 1.20 (m, 120H), 0.88 (t, 18H).

¹³C-NMR (75MHz, CDCl₃) δ(ppm): 167.99, 159.86, 159.62, 135.31, 133.53, 128.27, 127.90, 127.71, 127.02, 125.85, 123.88, 123.82, 123.67, 123.31, 33.39, 28.69, 28.45, 26.78, 26.41, 26.12, 23.21, 19.46, 10.89.

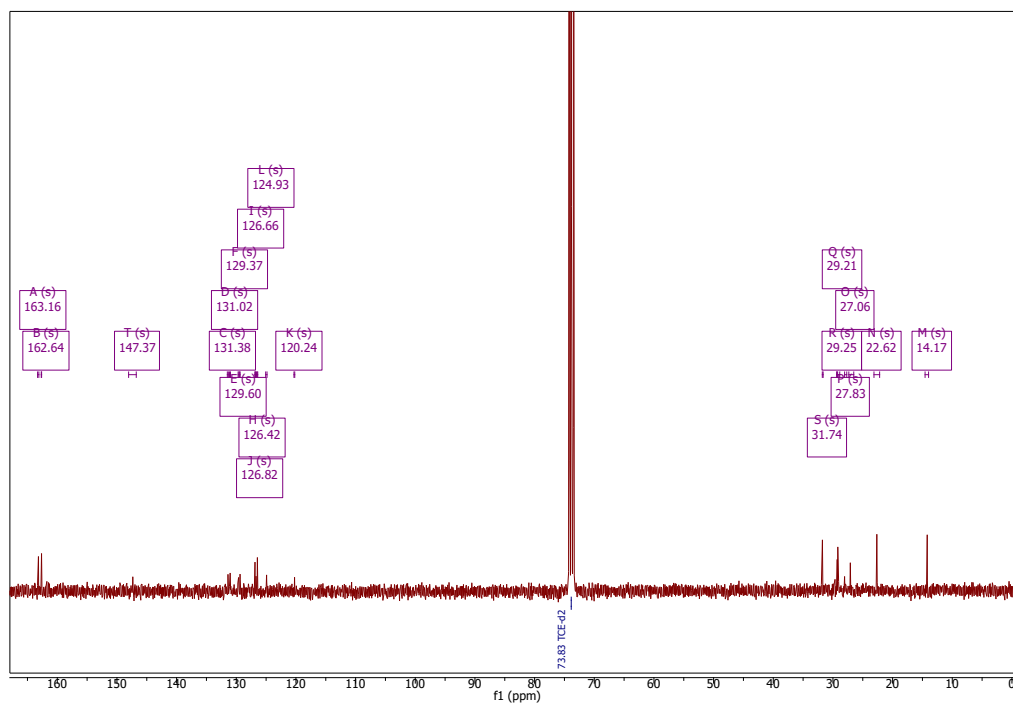
FTIR (ATR) $\tilde{\nu}$ (cm⁻¹): 2963.42, 2922.44, 2856.63, 1711.28, 1666.78, 1666.78, 1524.67, 1456.39, 1414.42, 1371.78, 1340.07, 1323.74, 1254.04, 1250.49, 1179.79, 1151.15, 1092.65, 1022.75, 803.67.

MS (MALDI): Found C₁₃₅H₁₇₁N₉O₁₂ [M]⁺ 2111.514 m/z; Calcd C₉₀H₇₈N₆O₁ [M]⁺ 2111.9 m/z.

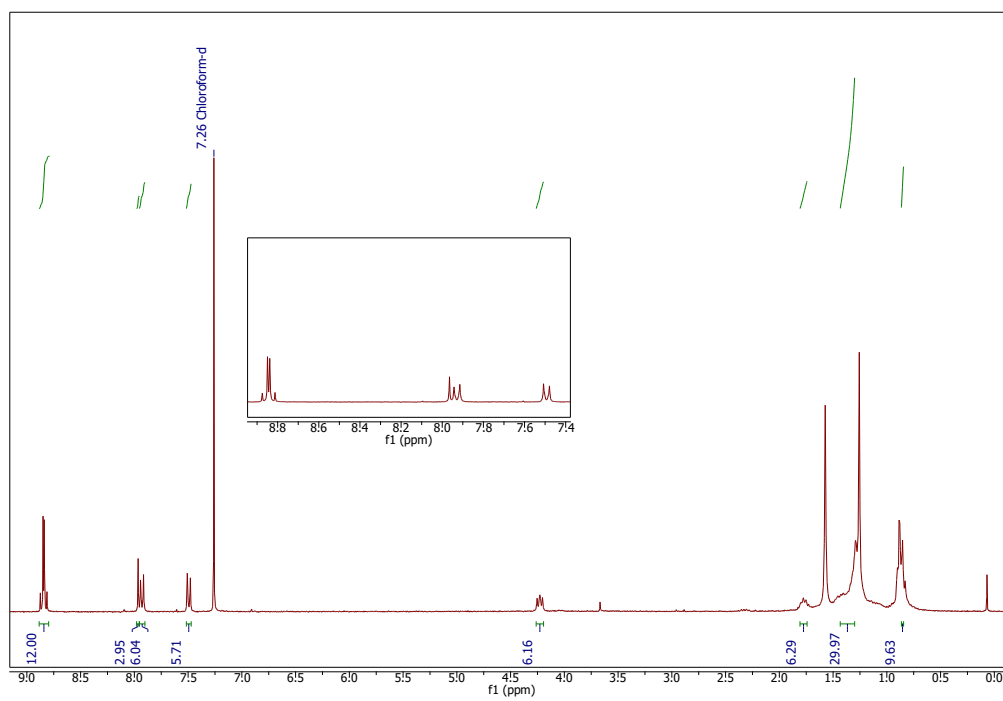
Melting point 186-187 °C.



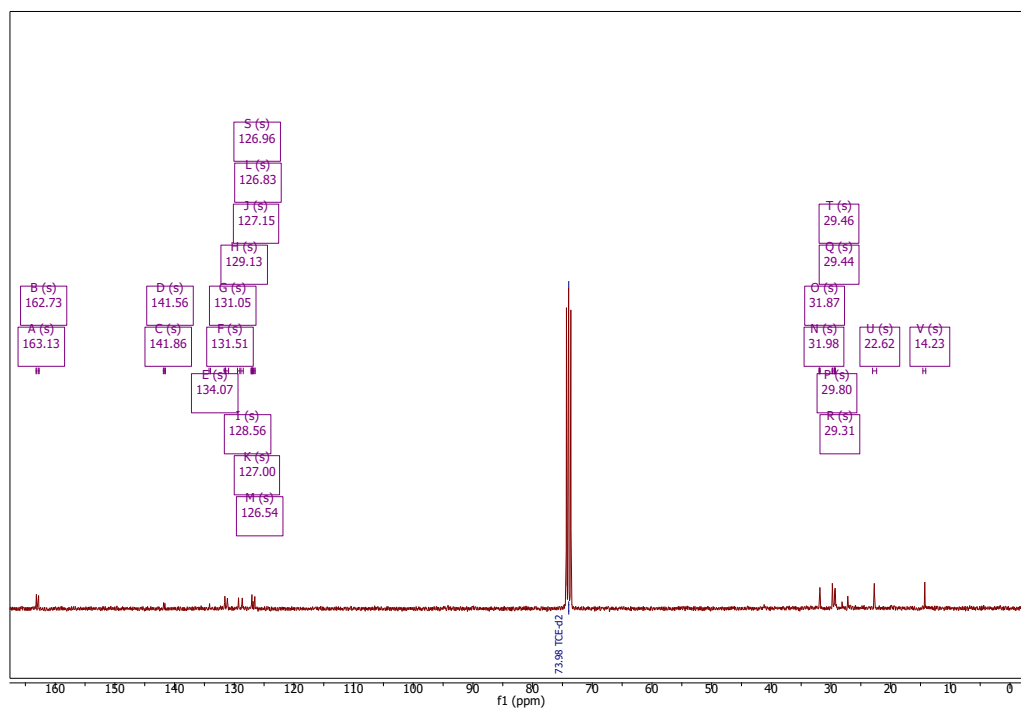
TAPA-NDI-A ^1H NMR spectrum (CHCl_3).



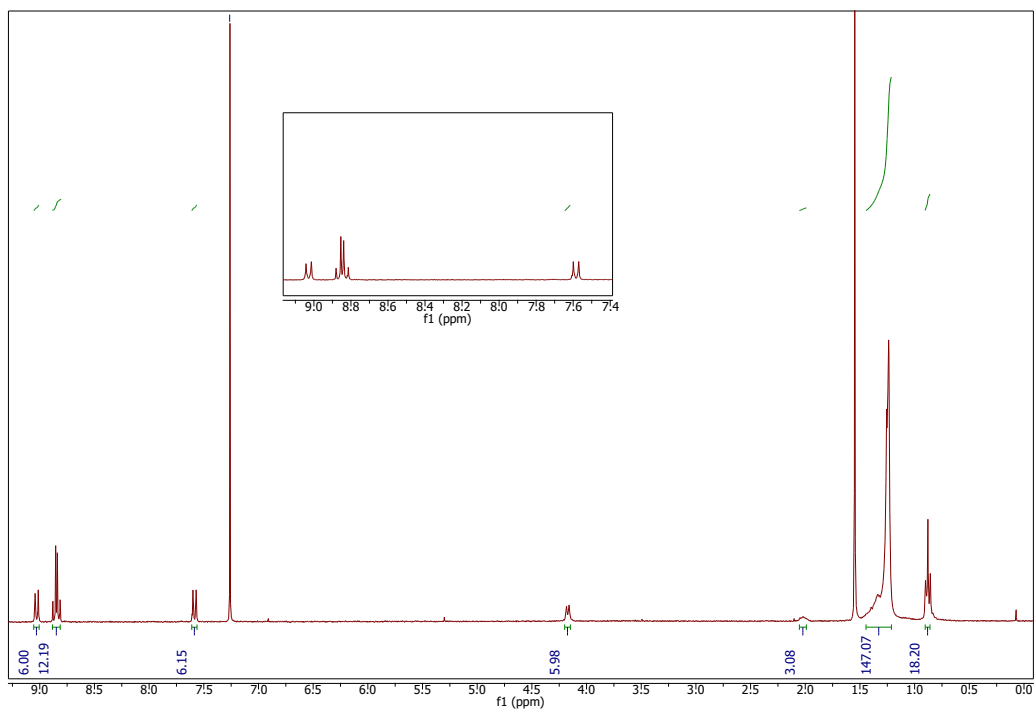
TAPA-NDI-A ¹³C NMR spectrum (TCE-d₂).



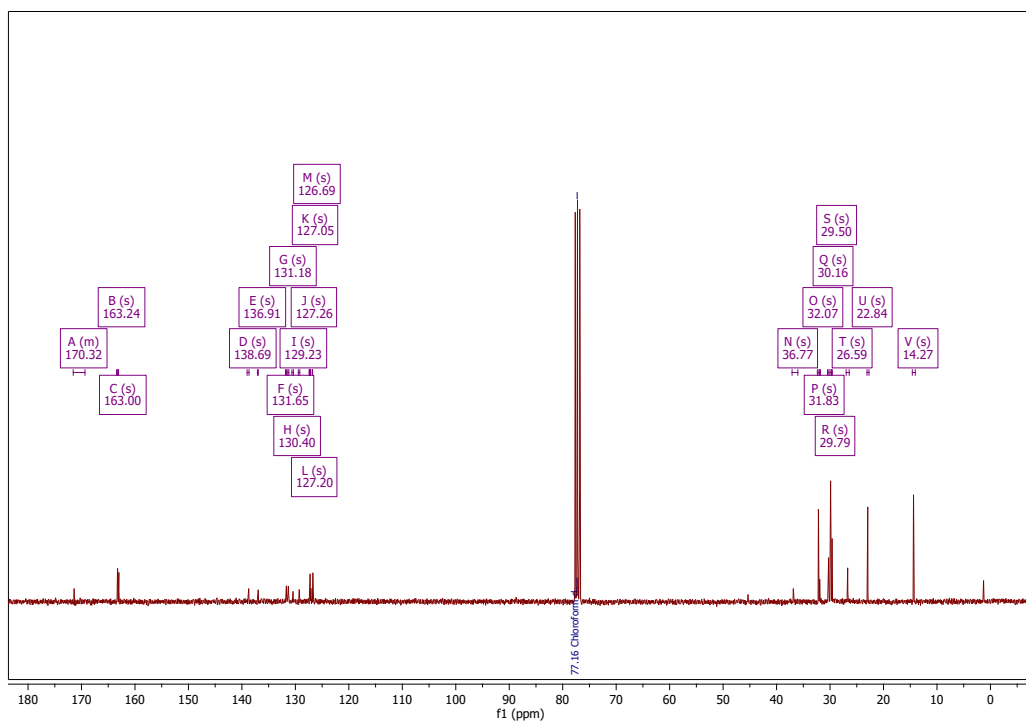
TAPB-NDI-A ¹H NMR spectrum (CHCl₃).



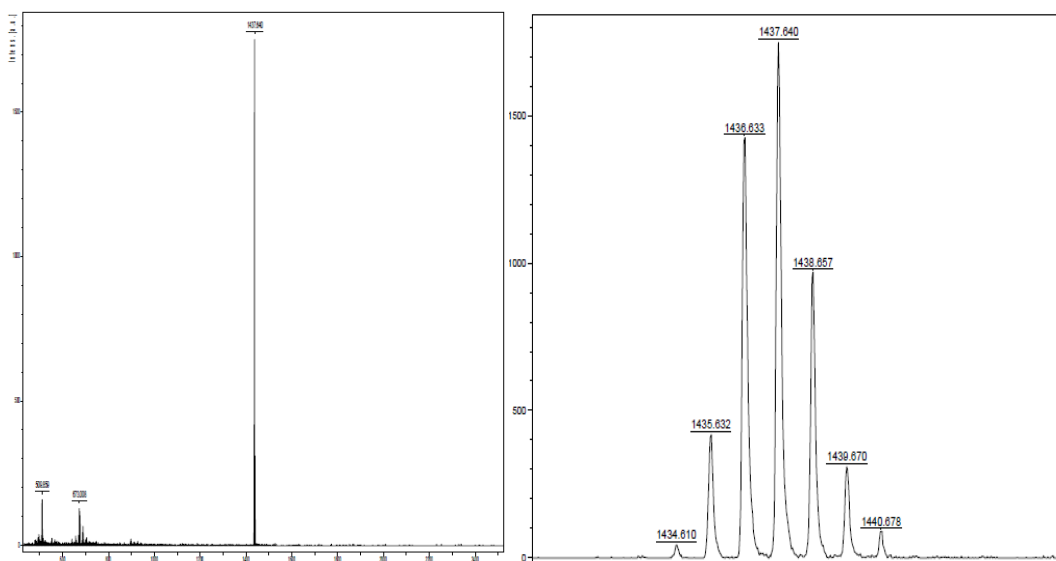
TAPB-NDI-A ^{13}C NMR spectrum (TCE-d_2).



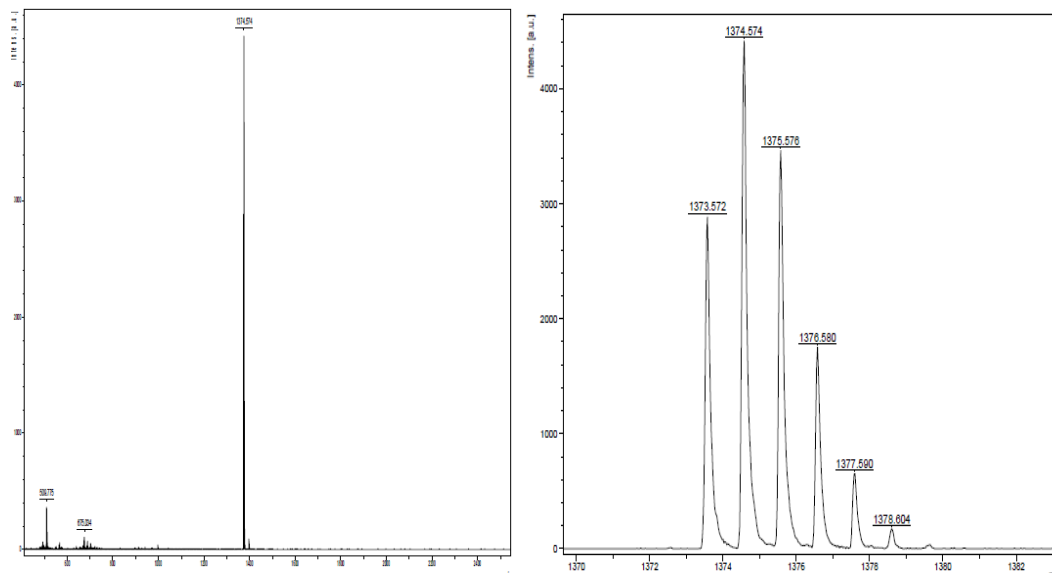
TAPT-NDI-A ^1H NMR spectrum (CHCl_3).



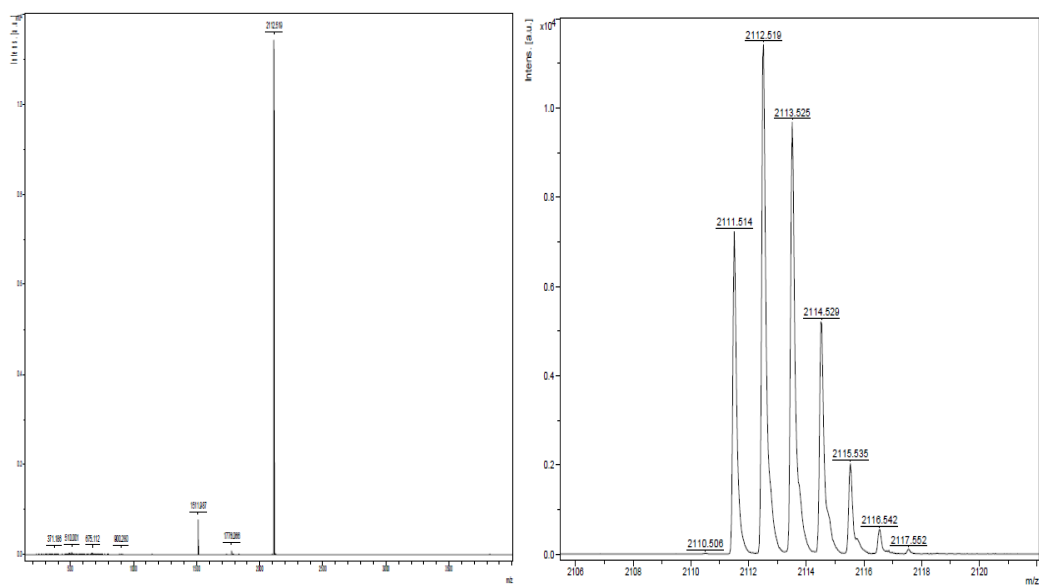
TAPT-NDI-A ^{13}C NMR spectrum (CDCl_3).



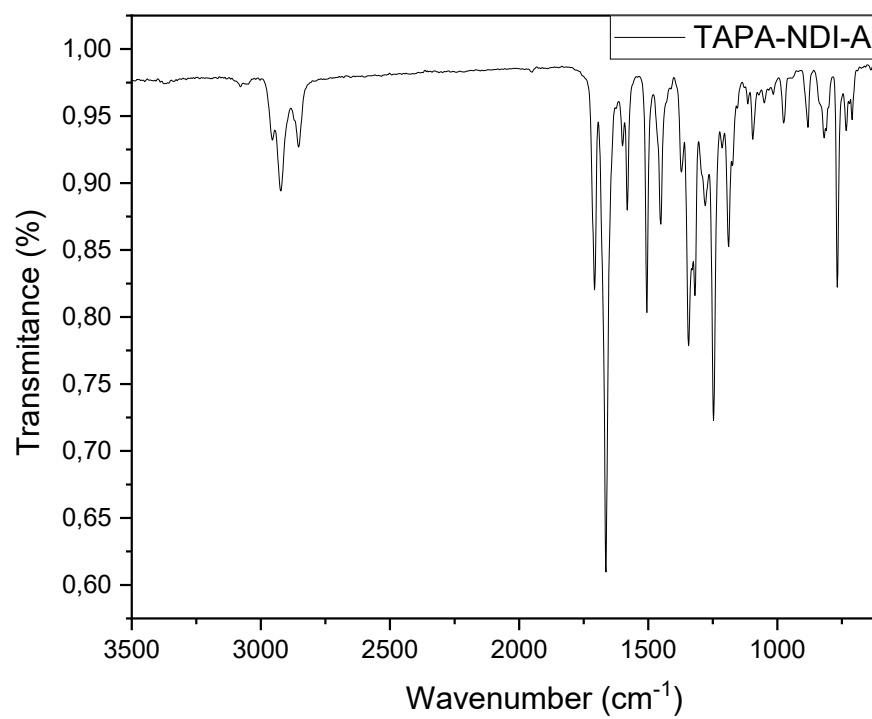
TAPA-NDI-AMALDI-HRMS (m/z) spectrum.



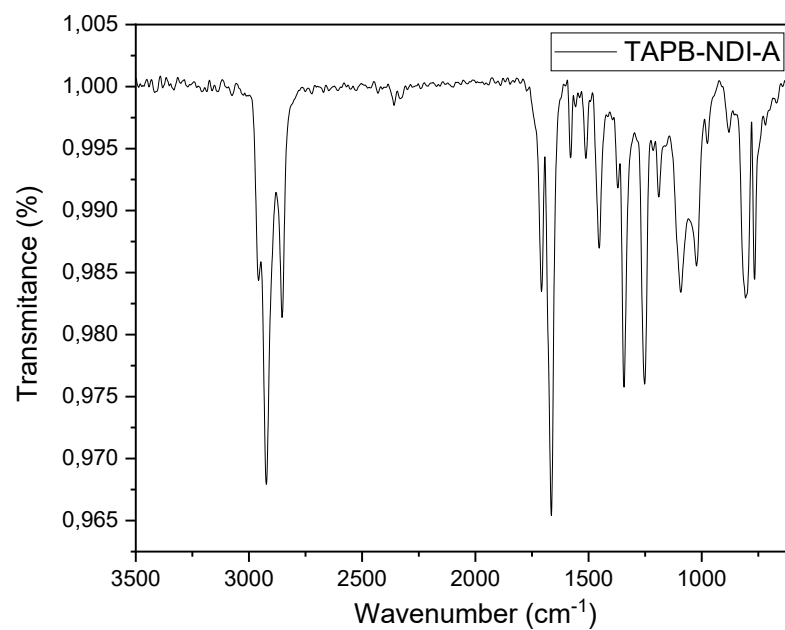
TAPB-NDI-AMALDI-HRMS (m/z) spectrum.



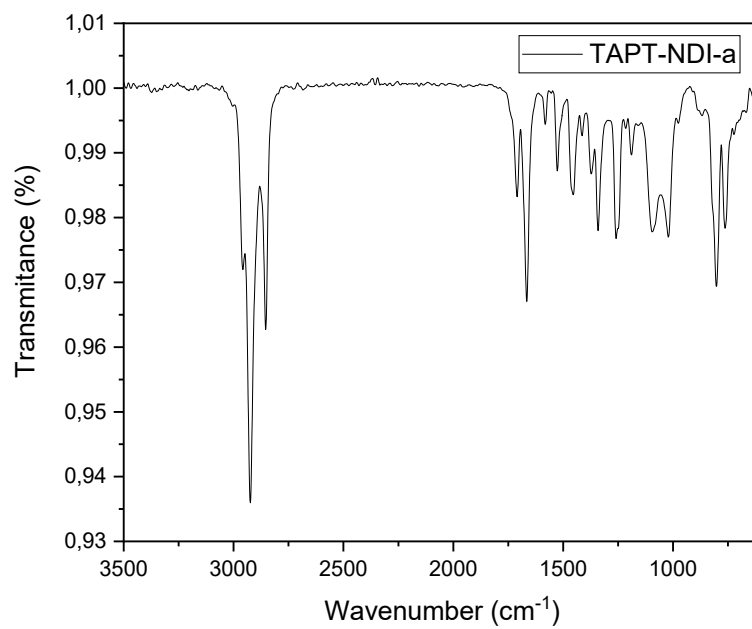
TAPT-NDI-AMALDI-HRMS (m/z) spectrum.



TAPA-NDI-A FTIR spectrum.



TAPB-NDI-A FTIR spectrum.



TAPT-NDI-A FTIR spectrum.

References

- [1] Khan, Q. U., Lu, J., Guo, J., Tian, G., Qi, S., Wu, D., *Dyes and Pigments* (2018) **149**, 193. <https://www.sciencedirect.com/science/article/pii/S0143720817316583>
- [2] Gomes, R., Bhanja, P., Bhaumik, A., *Chemical Communications* (2015) **51** (49), 10050. <http://dx.doi.org/10.1039/C5CC02147B>
- [3] de la Peña Ruigómez, A., Rodríguez-San-Miguel, D., Stylianou, K. C., Cavallini, M., Gentili, D., Liscio, F., Milita, S., Roscioni, O. M., Ruiz-González, M. L., Carbonell, C., MasPOCH, D., Mas-Ballesté, R., Segura, J. L., Zamora, F., *Chemistry – A European Journal* (2015) **21** (30), 10666. <https://doi.org/10.1002/chem.201501692>
- [4] Lv, J., Tan, Y.-X., Xie, J., Yang, R., Yu, M., Sun, S., Li, M.-D., Yuan, D., Wang, Y., *Angewandte Chemie International Edition* (2018) **57** (39), 12716. <https://onlinelibrary.wiley.com/doi/abs/10.1002/anie.201806596>
- [5] Royuela, S., Martínez-Periñán, E., Arrieta, M. P., Martínez, J. I., Ramos, M. M., Zamora, F., Lorenzo, E., Segura, J. L., *Chemical Communications* (2020) **56** (8), 1267. <http://dx.doi.org/10.1039/C9CC06479F>